OPEN ACCESS



Changing-look Active Galactic Nuclei from the Dark Energy Spectroscopic Instrument. I. Sample from the Early Data

```
Wei-Jian Guo<sup>1</sup>, Hu Zou<sup>1</sup>, Victoria A. Fawcett<sup>2</sup>, Rebecca Canning<sup>3</sup>, Stephanie Juneau<sup>4</sup>, Tamara M. Davis<sup>5</sup>,
 David M. Alexander 0, Linhua Jiang 0, Jessica Nicole Aguilar Steven Ahlen 0, David Brooks 10, Todd Claybaugh Axel de la Macorra 11, Peter Doel 10, Kevin Fanning 12, Jaime E. Forero-Romero 13,14, Satya Gontcho A Gontcho Klaus Honscheid 12,15,16, Theodore Kisner 10, Anthony Kremin 10, Martin Landriau 10, Aaron Meisner 17, Aaron Meisner 18, Aaron Meisner 18, Aaron Meisner 18, Aaron Meisner 19, Aaron Meisner 
Ramon Miquel<sup>18,19</sup>, John Moustakas<sup>20</sup>, Jundan Nie<sup>1</sup>, Zhiwei Pan<sup>7,21</sup>, Claire Poppett<sup>8,22,23</sup>, Francisco Prada<sup>24</sup>, Mehdi Rezaie<sup>25</sup>, Graziano Rossi<sup>26</sup>, Małgorzata Siudek<sup>27</sup>, Eusebio Sanchez<sup>28</sup>, Michael Schubnell<sup>29,30</sup>, Hee-Jong Seo<sup>31</sup>,
                                                                      Jipeng Sui<sup>1,32</sup>, Gregory Tarlé<sup>30</sup>, and Zhimin Zhou<sup>1</sup>
  1 Key Laboratory of Optical Astronomy, National Astronomical Observatories, Chinese Academy of Sciences, Beijing 100012, People's Republic of China
                                                                                                guowj@bao.ac.cn, zouhu@nao.cas.cn
                                                <sup>2</sup> School of Mathematics, Statistics and Physics, Newcastle University, Newcastle NE1 7RU, UK
                             <sup>3</sup> Institute of Cosmology & Gravitation, University of Portsmouth, Dennis Sciama Building, Portsmouth, PO1 3FX, UK
                                                                         NSF's NOIRLab, 950 N. Cherry Avenue, Tucson, AZ 85719, USA
                                                         <sup>5</sup> School of Mathematics and Physics, University of Queensland, QLD 4072, Australia
                             <sup>6</sup> Centre for Extragalactic Astronomy, Department of Physics, Durham University, South Road, Durham, DH1 3LE, UK
                                     Kavli Institute for Astronomy and Astrophysics, Peking University, Beijing 100871, People's Republic of China
                                                         Lawrence Berkeley National Laboratory, 1 Cyclotron Road, Berkeley, CA 94720, USA
                                                     Physics Dept., Boston University, 590 Commonwealth Avenue, Boston, MA 02215, USA
                                      Department of Physics & Astronomy, University College London, Gower Street, London, WC1E 6BT, UK
                                               Instituto de Física, Universidad Nacional Autónoma de México, Cd. de México C.P. 04510, Mexico

12 The Ohio State University, Columbus, OH 43210, USA
                                <sup>13</sup> Departamento de Física, Universidad de los Andes, Cra. 1 No. 18A-10, Edificio Ip, CP 111711, Bogotá, Colombia
                              <sup>14</sup> Observatorio Astronómico, Universidad de los Andes, Cra. 1 No. 18A-10, Edificio H, CP 111711 Bogotá, Colombia
               15 Center for Cosmology and AstroParticle Physics, The Ohio State University, 191 West Woodruff Avenue, Columbus, OH 43210, USA

16 Department of Physics, The Ohio State University, 191 West Woodruff Avenue, Columbus, OH 43210, USA

17 NORTH AND OSO N. Charm. Acro. AZ 85710, USA
                                                                             NSF's NOIRLab, 950 N. Cherry Ave., Tucson, AZ 85719, USA
                                    <sup>18</sup> Institució Catalana de Recerca i Estudis Avançats, Passeig de Lluís Companys, 23, E-08010 Barcelona, Spain
     19 Institut de Física d'Altes Energies (IFAE), The Barcelona Institute of Science and Technology, Campus UAB, E-08193 Bellaterra, Barcelona, Spain
                                            Department of Physics and Astronomy, Siena College, 515 Loudon Road, Loudonville, NY 12211, USA
                                   Department of Astronomy, School of Physics, Peking University, Beijing 100871, People's Republic of China
                                           Space Sciences Laboratory, University of California, Berkeley, 7 Gauss Way, Berkeley, CA 94720, USA

23 University of California, Berkeley, 110 Sproul Hall #5800, Berkeley, CA 94720, USA
                                          <sup>24</sup> Instituto de Astrofísica de Andalucía (CSIC), Glorieta de la Astronomía, s/n, E-18008 Granada, Spain
                                                  Department of Physics, Kansas State University, 116 Cardwell Hall, Manhattan, KS 66506, USA
                                                 Department of Physics and Astronomy, Sejong University, Seoul, 143-747, Republic of Korea
                                  <sup>27</sup> Institute of Space Sciences (ICE, CSIC), Campus UAB, Carrerde Can Magrans, s/n, E-08193 Barcelona, Spain
                                                                            <sup>28</sup> CIEMAT, Avenida Complutense 40, E-28040 Madrid, Spain
                                                              Department of Physics, University of Michigan, Ann Arbor, MI 48109, USA
                                                                                      University of Michigan, Ann Arbor, MI 48109, USA
                                                           <sup>31</sup> Department of Physics & Astronomy, Ohio University, Athens, OH 45701, USA
  <sup>32</sup> School of Astronomy and Space Science, University of Chinese Academy of Sciences, 19A Yuquan Road, Beijing 100049, People's Republic of China
                                     Received 2023 July 12; revised 2023 November 17; accepted 2023 November 18; published 2024 January 29
```

Abstract

Changing-look active galactic nuclei (CL AGNs) can be generally confirmed by the emergence (turn-on) or disappearance (turn-off) of broad emission lines (BELs), associated with a transient timescale (about $100 \sim 5000$ days) that is much shorter than predicted by traditional accretion disk models. We carry out a systematic CL AGN search by crossmatching the spectra coming from the Dark Energy Spectroscopic Instrument and the Sloan Digital Sky Survey. Following previous studies, we identify CL AGNs based on H α , H β , and Mg II at $z \leq 0.75$ and Mg II, C III], and C IV at z > 0.75. We present 56 CL AGNs based on visual inspection and three selection criteria, including 2 H α , 34 H β , 9 Mg II, 18 C III], and 1 C IV CL AGN. Eight cases show simultaneous appearances/disappearances of two BELs. We also present 44 CL AGN candidates with significant flux variation of BELs, but remaining strong broad components. In the confirmed CL AGNs, 10 cases show additional CL candidate features for different lines. In this paper, we find: (1) a 24:32 ratio of turn-on to turn-off CL AGNs; (2) an upper-limit transition timescale ranging from 330 to 5762 days in the rest frame; and (3) the majority of CL AGNs follow the bluer-when-brighter trend. Our results greatly increase the current CL census (\sim 30%) and would be conducive to exploring the underlying physical mechanism.

Unified Astronomy Thesaurus concepts: Active galaxies (17); Accretion (14); Active galactic nuclei (16); Supermassive black holes (1663); Catalogs (205)

Supporting material: figure set

1. Introduction

In the unification paradigm, different types of active galactic nuclei (AGNs) or quasars³³ are classified by their orientation relative to the line of sight and the present significant flux variation (about 10%-30%) across the entire electromagnetic spectrum on monthly to annual timescales (Antonucci 1993; Vanden Berk et al. 2004). The broad-line region (BLR) is located close to the central supermassive black hole (a few light-days' to light-months' distance). The ionized gas of the BLR emits broad emission lines (BELs) with a smaller flux variation amplitude than the continuum (Du & Wang 2019; Kaspi et al. 2000). These BELs (in particular, the Balmer lines) have been found to respond to continuum variations with a time delay. This time delay has been used, in a technique known as reverberation mapping, to study the geometry and kinematics of the BLR and measure the central black hole mass (Blandford & McKee 1982; Peterson 1993; Bentz et al. 2009; Ho & Kim 2014; Li et al. 2018; Zhang et al. 2019; Lu et al. 2021; Bao et al. 2022). The variation of BEL features is therefore an effective tool for studying the formation of the BLR and the evolution of the AGN. However, Mg II and C IV are less responsive to the continuum variation than Balmer lines, because of their intrinsic properties, such as weak response, the extended BLR size, or outflows (Richards et al. 2011; Sun et al. 2018; MacLeod et al. 2019; Yu et al. 2021).

The changing-look (CL) phenomenon was originally used to characterize X-ray-detected AGNs that change between Compton-thick and Compton-thin (Matt et al. 2003; Temple et al. 2023). In the optical band, the CL phenomenon is a surprising and unusual event in which the BELs in AGN spectra appear or disappear (from Type 1 to Type 2 or vice versa) within just a few months or years. In low-redshift AGNs (z < 0.1), CL could also refer to the transition between intermediate types (such as Type 1.2, Type 1.5, Type 1.8, and Type 1.9) that is determined by the flux ratio between H β and $H\alpha$ or $[OIII]^{34}$ (Osterbrock 1981; Cohen et al. 1986; Winkler 1992; Denney et al. 2014; Li et al. 2022b). The discovery of the first CL quasar, SDSS J015957.64+003310.5, by LaMassa et al. (2015), which underwent a dramatic change from Type 1 to Type 1.9 in just 10 yr, poses a challenge to our understanding of the AGN unified model and the widely accepted viscous heating timescale (hundreds of years) of a steady accretion disk (Shakura & Sunyaev 1973; Cackett et al. 2007; Runnoe et al. 2016; Tie & Kochanek 2018; Guo et al. 2022). The study of CL AGN evolution can also shed light on the growth and feedback processes of supermassive black holes and the impact of AGNs on their host galaxies (Ho 2005; Wang & Zhang 2007; Zhuang & Ho 2019; Jin et al. 2022).

Over 100 CL AGNs have been discovered based on their Balmer-line profile transitions (MacLeod et al. 2016; Gezari et al. 2017; Sheng et al. 2017; Frederick et al. 2019; Green et al.

2022; Hon et al. 2022; Zeltyn et al. 2022; Chen et al. 2023; Yang et al. 2023), and dozens of CL AGNs have also been identified based on transitions in Mg II, C III], and C IV (Guo et al. 2019, 2020; Ross et al. 2020). However, the nature and frequency of CL AGNs are still not well understood, and many questions remain unanswered. For instance, the occurrence rate of CL events in AGNs and the relationship between CL AGNs and normal AGNs are unclear. Additionally, the mechanisms responsible for these changes are yet to be fully understood. Three commonly proposed possible causes are: (1) changes in the central gas density due to the variation of the energy radiation intensity from the nucleus or accelerating outflows (Shapovalova et al. 2010; LaMassa et al. 2015; Ricci & Trakhtenbrot 2023); (2) a rapid increase or decrease of the gas density and accretion rate in the compact region originating from tidal disruption events (Blanchard et al. 2017; Li et al. 2022a); and (3) accretion rate changes caused by BLR evolution, accretion disk instability, or temporary accretion events (Esin et al. 1997; Elitzur & Ho 2009; Dexter & Agol 2011; Elitzur et al. 2014; MacLeod et al. 2019; Śniegowska & Czerny 2020). CL AGNs may be attributed to various mechanisms or influenced by multiple physical processes.

To better understand the physical mechanism behind the CL phenomenon, it is essential and pressing to conduct further spectral monitoring of previously discovered objects and to additionally search for new CL AGNs. There are several effective methods to hunt for CL AGNs, including: (1) crossmatching AGN spectra in multiple-epoch large-area spectroscopic projects, such as those performed by MacLeod et al. (2016), Yang et al. (2018), and Green et al. (2022); and (2) identifying potential candidates through follow-up spectroscopic observations, by detecting extremely unusual variability in optical or mid-IR light curves, as seen in studies by Sheng et al. (2017), MacLeod et al. (2019), and Graham et al. (2020). The Dark Energy Spectroscopic Instrument (DESI) offers an excellent opportunity to hunt for CL AGNs, as it boasts a large field of view, high spectral resolution, and high data generation efficiency (as described in detail in Section 2). Another advantage of DESI is the high sensitivity, allowing for the identification of lower-luminosity accretion events.

We aim to explore the physical mechanism behind CL AGNs and improve the completeness of the current sample. To achieve this, we will utilize the spectroscopic data from DESI and the Sloan Digital Sky Survey (SDSS). The DESI project will provide nearly three million quasar spectra over the next 5 yr, while the SDSS project has already identified 750,414 quasars. By crossmatching the AGN spectra from these two projects, we will be able to compile a large sample of CL AGNs and study their behaviors. Previous studies have primarily focused on Balmer-line (H α and H β) CL AGNs at redshifts z < 0.7 (MacLeod et al. 2016, 2019; Yang et al. 2018; Graham et al. 2020; Green et al. 2022). Since high-ionization BELs are thought to connect the inner region of the accretion disk and the BLR (Guo et al. 2019; Ross et al. 2020), we aim to study CL AGNs for several major BELs at all redshifts, including $H\alpha$, $H\beta$, Mg II, C III], and C IV. Therefore, we will

 $^{^{\}overline{33}}$ CL quasars refer to the most luminous cases with bolometric luminosities $L_{\rm bol} > 10^{44}\,{\rm erg\,s^{-1}}$, but we do not distinguish based on luminosity in this work and use CL AGN for the full range.

 $^{^{34}}$ In this paper, we define an intermediate-type transition as a CL candidate where the broad component is still present.

divide the sample into two parts, based on redshift ($z \le 0.75$ and z > 0.75), to search for CL AGNs in both the rest-frame UV and optical wavelengths. The results of this study will provide crucial insights into the properties of CL AGNs and contribute to our understanding of the AGN population.

The paper is structured as follows. In Section 2, we describe the data from the DESI and SDSS projects. Section 3 outlines the process for selecting our target sample, including the use of both visual inspection (VI) and spectral variability definitions to identify CL objects. In Section 4, we present our findings on the five BEL CL behaviors, and upper-limit timescales, and discuss potential physical origins. The paper concludes with a summary in Section 5. Throughout, we adopt a Λ CDM cosmology with $H_0 = 67 \, \mathrm{km \, s^{-1} \, Mpc^{-1}}$, $\Omega_{\Lambda} = 0.68$, and $\Omega_m = 0.32$, as reported by Planck Collaboration et al. (2020).

2. Data

2.1. DESI

DESI³⁵ uses the NOIRLab 4 m Mayall telescope (8 deg² field view) at Kitt Peak with the aim of constraining the nature of dark energy and probing cosmological distances through the baryon acoustic oscillation technique (Levi et al. 2013; DESI Collaboration et al. 2016a, 2016b; Miller et al. 2023; Schlafly et al. 2023; Silber et al. 2023; D. Kirkby et al. 2024, in preparation; A. Raichoor et al. 2024, in preparation). DESI is carrying out the largest ever multiobject and high-efficiency spectral survey (5000 spectra in a single exposure) and plans to measure 40 million galaxies and quasars within 5 yr (DESI Collaboration et al. 2016a, 2022; Allende Prieto et al. 2020; Zhou et al. 2020; Raichoor et al. 2023). The DESI program will accumulate about three million quasar spectra to measure largescale structures in the main survey (Ruiz-Macias et al. 2020; Yèche et al. 2020; Hahn et al. 2023; Lan et al. 2023). Since the limiting magnitude of DESI in the r band reaches about 23 mag, DESI has a unique opportunity to discover fainter and higher-redshift quasars than any previous survey, quadrupling the number of quasars discovered by SDSS (Zou et al. 2018; Alexander et al. 2023; Chaussidon et al. 2023). Besides the strengths in quantity and depth, three optical channels (blue: 3600–5900 Å; green: 5660–7220 Å; and red: 7470–9800 Å) also provide an excellent spectral resolution (blue: $R \sim 2100$; green: $R \sim 3200$; and red: $R \sim 4100$; Abareshi et al. 2022).

Guy et al. (2023) describe the spectroscopic data processing pipeline in detail and the references therein present the target selection and validation (Alexander et al. 2023; Cooper et al. 2023; Lan et al. 2023; Myers et al. 2023; Raichoor et al. 2023; Zhou et al. 2023). Before the start of the main survey, data from the Survey Validation (SV) were visually inspected to check the spectroscopic quality and redshift reliability (DESI Collaboration et al. 2023a, 2023b), improve the standard DESI spectroscopic pipelines, such as the "Redrock" and "afterburner" codes, and reduce the number of misclassified quasars (Alexander et al. 2023).

With a large sample of quasars and high-quality spectra, DESI offers unprecedented advantages for identifying CL AGNs. Since DESI has the advantage of observing fainter AGNs than SDSS, more turn-off CL AGNs are expected to be discovered. In this project, we used 347,201 quasar spectra and 2,955,168 galaxy spectra reduced by the DESI pipeline (based

on the SPECTYPE from "Redrock") with ZWARN = 0 (S. Bailey et al. 2024, in preparation; Brodzeller et al. 2023), indicating reliable spectroscopic redshift measurements, which contain SV (named as "fuji") and the first two months of Year 1 data (named as "guadalupe"; DESI Collaboration et al. 2023b). The data of "fuji" are published as part of the Early Data Release, and "guadalupe" will be published at the same time as Data Release 1 (DR1; Alexander et al. 2023; DESI Collaboration et al. 2023a; Lan et al. 2023; Raichoor et al. 2023).

2.2. SDSS/BOSS/eBOSS

In addition to the DESI data, we used the SDSS³⁶ spectroscopic data, which cover a large region of the sky and have millions of spectra of galaxies and quasars (Gunn et al. 2006). The SDSS spectroscopic database provides additional high-quality data for the comparison and validation of the DESI redshift measurement. SDSS is carried out on a 2.5 m Sloan telescope at Apache Point Observatory and has provided a large database of quasar and galaxy spectra through four stages of projects (SDSS-I, SDSS-II, SDSS-III/BOSS, and SDSS-IV/ eBOSS; Abazajian et al. 2009; Alam et al. 2017; Lyke et al. 2020). The spectra have a wavelength coverage of 3900–9100 Å or 3600–10400 Å and a resolution of $R \sim 2000$ for quasars and galaxies (Eisenstein et al. 2011; Smee et al. 2013). All the SDSS spectra are reduced with the SDSS-I/II and BOSS data pipelines (Stoughton et al. 2002; Bolton et al. 2012). In this study, we have used 750,414 quasar spectra from the SDSS Data Release 16 Quasar (DR16Q) catalog released by Lyke et al. (2020) and 4,930,400 galaxy spectra from DR16 (Ahumada et al. 2020).

2.3. Image Survey and Light Curve

Motivated by the target selection for DESI, the DESI Legacy Surveys³⁷ team utilized a deep and large-area image survey (Dey et al. 2019). The survey comprised three projects: the Dark Energy Camera Legacy Survey, the Beijing–Arizona Sky Survey, and the Mayall *z*-band Legacy Survey, which covered approximately 14,000 deg² of extragalactic sky, including 9900 deg² in the North Galactic Cap and 4400 deg² in the South Galactic Cap (Flaugher et al. 2015; Zhou et al. 2023; D. Schlegel et al. 2024, in preparation). The survey was conducted using three optical/IR bands, reaching approximate AB magnitudes of g = 24.0, r = 23.4, and z = 22.5 (Dey et al. 2019). We used the DESI Legacy Survey photometric magnitude to describe the distribution of the final CL AGN sample.

To test the flux calibration of the target using the long-term light curve of photometry, we utilized various surveys and facilities, including the Catalina Real-time Transient Survey (CRTS; Drake et al. 2009), Pan-STARRS1 (PS1; Chambers et al. 2016), the Palomar Transient Factory (PTF; Law et al. 2009), and the Zwicky Transient Facility (ZTF; Masci et al. 2019). First, we obtained the magnitude of pseudophotometry by convolving the target's spectrum with the corresponding filter response function. This process allows us to calculate the observed magnitude in a specific bandpass. By analyzing the consistency between the pseudophotometry magnitude and the observed light curve, we can identify any discrepancies or

https://www.desi.lbl.gov/

³⁶ https://www.sdss.org/

³⁷ http://legacysurvey.org/

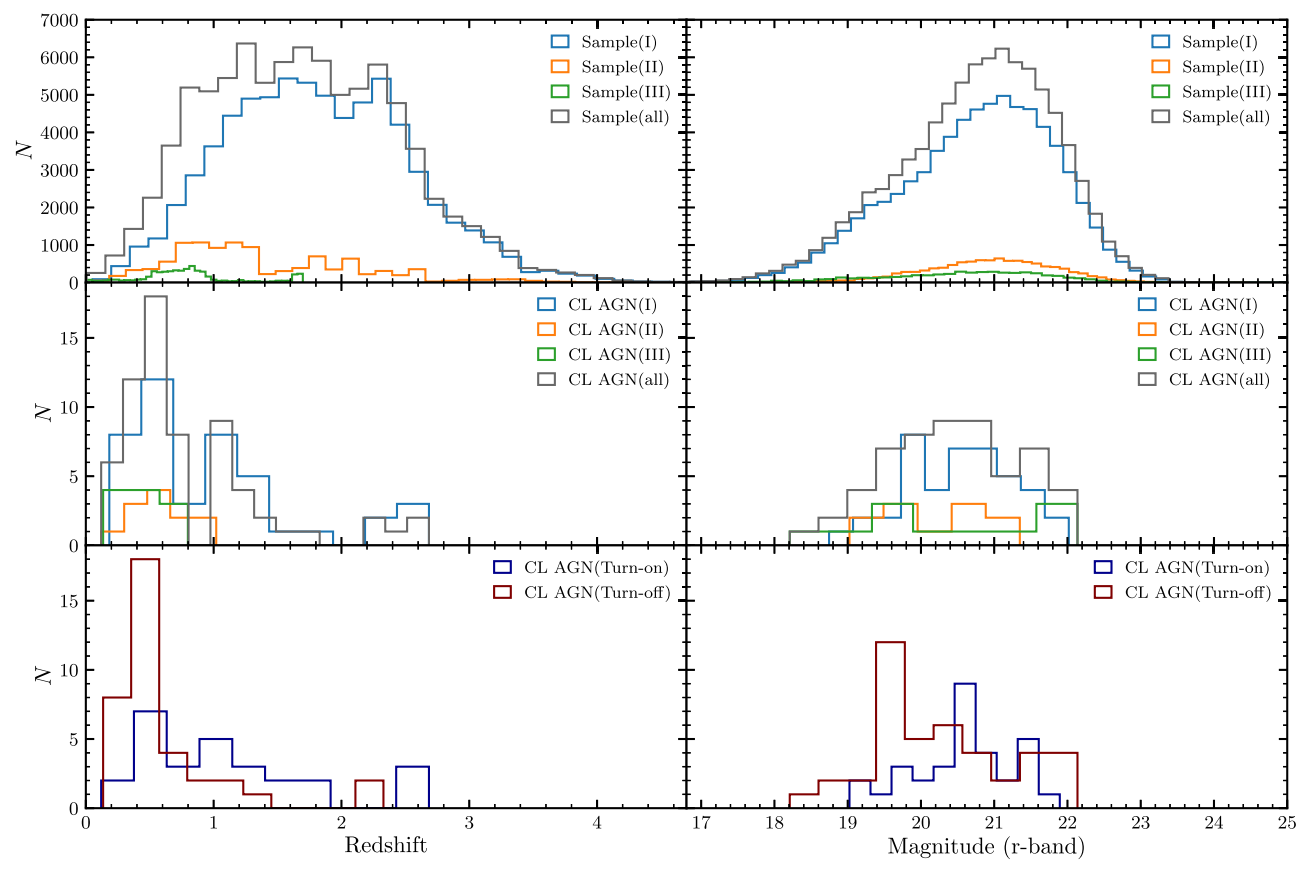


Figure 1. The histograms for the redshift (left) and *r*-band magnitude (right) from the DESI Legacy survey are shown. The top panels display the total parent sample (gray) and the three crossmatched groups (blue, orange, and green). The middle panels represent the distributions of CL AGNs found in the three crossmatched groups. The bottom panels show the distributions of CL AGNs with the transition states of turn-on (dark blue) and turn-off (maroon). Note that the *r*-band magnitude refers to the mean magnitude obtained from the image of the DESI Legacy Survey, which encompasses the period from 2014 to 2018.

inconsistencies that may indicate calibration issues or instrument problems affecting the identification of CL AGNs, such as SDSS fiber drop. We remove 121 spurious CL AGNs to ensure the reliability of the final CL AGN sample in Section 3.4.

2.4. Data Preprocessing

To facilitate the subsequent analyses, including spectrum inspection, defining the change of the flux threshold, and sample selection, we corrected the spectra for galactic extinction by using the galactic extinction curve of Fitzpatrick (1999), by assuming $R_V = 3.1$. After that, we shifted the spectrum to the rest frame.

Since the spectra of SDSS and DESI have different wavelength coverages and resolutions, the flux variation cannot be obtained directly by subtraction with two original spectra. Therefore, we rebin both spectra into the same wavelength grid for flux and its variance (2 Å per pixel) to be able to reliably compare and subtract the SDSS and DESI spectra.

3. Sample Selection

Although DESI has more than one spectrum for some targets, we only use one epoch of DESI for each target and remove any duplicates. This approach does not affect the results of our study, as the time interval between the different epochs of DESI spectra is within 1 yr, which is usually shorter than the timescale of most CL objects (for more details, see Section 4.2).

The sample selection process for the CL AGNs in this study involves four steps: (1) build a parent sample of AGNs that are observed by both DESI and SDSS; (2) a first stage of the VI of spectra (both SDSS and DESI) to select CL candidates; (3) set the selection criteria with a variability definition to automatically identify the CL AGNs in the parent sample; (4) [O III]-based calibration for those AGNs at $z \leq 0.75$ to remove spurious objects; and (5) a second stage of the VI of spectra to remove spurious CL AGNs by comparing the long-term light curve with the pseudophotometry obtained.

We define the parent sample in Section 3.1, describe the target selection and spectral classification diagnosis by VI in Section 3.2, identify the final CL catalog by the spectral variability definition in Section 3.3, and carry out an [O III]-based calibration and pseudophotometry check to remove spurious CL candidates in Section 3.4.

3.1. Parent Sample

We used all the spectra from the DESI catalog and the SDSS DR16 catalog to systematically search for the CL AGNs or candidates. To obtain a parent sample of AGNs with two epochs of spectra, we crossmatched the DESI spectra catalog with the SDSS catalog using a 1" separation, including both quasars and galaxies. After that, we obtained SDSS spectra of the matched sample through the Science Archive Server (SAS).³⁸ We note here that about 4% of spectra are missing

³⁸ https://dr16.sdss.org/optical/spectrum/search

Group I	Group II	Group III	N_{Σ}	Note
(1)	(2)	(3)	(4)	(5)
32,038	32,038	2,955,168	3,019,244	Quasars or galaxies in DESI
4239	1814	2547	8600	Crossmatch with DR16 within 1"
4073	1742	2181	7996	Available spectra
				through SAS
1	1	0	2	$H\alpha$ CL AGNs
21	3	10	34	$H\beta$ CL AGNs
2	1	3	6	Mg II CL AGNs
24	5	13	42	Total CL AGNs
0.59%	0.28%	0.59%	0.53%	CL AGN ratio
5	1	1	7	$H\alpha$ CL candidates
13	0	3	16	$H\beta$ CL candidates
5	1	4	10	Mg II CL candidates
23	2	8	33	Total CL candidates
0.56%	0.11%	0.37%	0.41%	CL candidate ratio

Notes. Column (1): AGN number in group I (DESI quasars and DR16 quasars). Column (2): AGN number in group II (DESI galaxies and DR16 quasars). Column (3): AGN number in group III (DESI quasars and DR16 galaxies). Column (4): the total number of AGNs from groups I, II, and III.

through SAS downloading, which is possibly due to the data quality.

Although the spectral classification pipelines of SDSS and DESI perform very efficiently, those objects with indistinct BEL characteristics or low-quality spectra could be leading to a misclassification of the spectral type (Alexander et al. 2023; Lan et al. 2023), especially for CL AGNs. As pointed out by many previous works (MacLeod et al. 2016; Yang et al. 2018; Green et al. 2022), the CL AGNs in a low state might be classified as galaxies because the BELs and blue continuum are no longer the dominant features. Therefore, we also included crossmatched results between AGNs with galaxies. Specifically, we divided the sample into three groups: group I (DESI quasars and DR16 quasars), group II (DESI galaxies and DR16 quasars), and group III (DESI quasars and DR16 galaxies). Finally, we built up a parent sample containing 82,653 matched AGN spectrum pairs (at least one source in the crossmatch is marked as an AGN). Figure 1 displays the redshift and r-band magnitude distributions of our parent sample and three different group samples.

Since previous works focus on the H α and H β CL phenomenon (MacLeod et al. 2016, 2019; Green et al. 2022), we divided the DESI spectra into two subsamples according to redshift to search for: (1) CL AGNs defined by H α , H β , and Mg II at $z \le 0.75$; and (2) CL AGNs defined by Mg II, C III], and C IV at z > 0.75. Another reason why we set z = 0.75 as the boundary between the two subsamples is that we can use [O III], which can be observed in SDSS spectra out to $z \sim 0.8$, to test the variability definition and estimate the final CL sample purity at z > 0.75, which required the inclusion of both H β and [O III] in the spectra (for more details, see Section 3.4). The number of AGNs in each of the three groups at $z \le 0.75$ and z > 0.75 are given in Tables 1 and 2, respectively. One might expect that a CL event would always have one epoch classified as an AGN and another as a galaxy (groups II and

Table 2 The Selection of CL AGNs and Candidates (Mg II, C III], and C IV) from DESI for z>0.75

Group I (1)	Group II (2)	Group III (3)	N_{sum} (4)	Note (5)
315,163	315,163	2,955,168	3,585,494	Quasars or galaxies in DESI
66,813	8925	2781	78,519	Crossmatch with DR16 within 1"
64,276	8213	2168	74,657	Available spectra through SAS
2	0	1	3	Mg II CL AGNs
16	2	0	18	C III] CL AGNs
1	0	0	1	C IV CL AGNs
19	2	1	22	Total CL AGNs
0.03%	0.02%	0.04%	0.03%	CL AGN ratio
4	1	1	6	Mg II CL candidates
10	0	0	10	C III] CL candidates
5	0	0	5	C IV CL candidates
19	1	1	21	Total CL candidates
0.03%	0.01%	0.04%	0.03%	CL candidate ratio

Note. The columns are the same as in Table 1.

III). However, we find that most often both are classified as AGNs (group I), since some CL AGNs in the dim state may not completely lose the broad components or these objects are still in the period of transition. More importantly, the quasar samples were classified by the standard pipeline "Redrock" or "QuasarNET" for both SDSS and DESI with about 86% completeness, which means some AGNs, such as host-galaxy-dominated AGNs, may be contained in the galaxy sample (Lyke et al. 2020; Alexander et al. 2023).

3.2. VI

Previous studies effectively diagnose CL AGNs based on the VI of large-area sky surveys (MacLeod et al. 2016, 2019; Yang et al. 2018; Green et al. 2022). Since the appearance or disappearance of BELs may be within a continuous process of spectral enhancement or weakening, it is a challenge to quantitatively describe the CL behavior with only two randomly sampled spectra. As mentioned by Green et al. (2022), a standard CL AGN target selection process starts with a VI to discard those spectra that have poor quality, large measurement errors, or wrong redshift identifications.

In this project, we also carry out the VI of the parent sample for three purposes. First, we need to remove those fake CL AGNs whose behavior might be caused by spectrum defects and/or disagreements between the SDSS and DESI redshifts. For example, the absorption associated with the C IV line (for example, broad-absorption-line AGNs; Rogerson et al. 2018) would impact the accuracy of the total BEL flux. Second, since the wavelength region of H α contains strong narrow emission lines (narrow H α and [N II]), the variation of the BEL flux determined by the integration method could be affecting the selection. We inspect all the H α CL candidates to confirm they are indeed CL AGNs in the selection program (see the details in Section 4).

Third, the final spectral variability definition that we apply is the automatic checker, which was established based on the results from the VI and the run on all the parent samples (see Section 3.3). In conclusion, the VI check is a crucial step in

Table 3The Information of Five BELs in AGNs

Line (1)	λ (Å) (2)	Window (Å) (3)	Window B1 (Å) (4)	Window B2 (Å) (5)	CL AGNs (6)	CL Candidates (7)	Mechanism (8)
CIV	1548.187, 1550.772	1510–1590	1460-1510	1590–1640	1	5	Collisional excitation
C III]	1906.683, 1908.734	1850-1970	1820-1850	1970-2000	18	10	Collisional excitation
Mg II	2795.528, 2802.705	2750-2850	2680-2720	2880-2920	9	16	Collisional excitation
$H\beta$	4861.333	4780-4940	4730-4770	5030-5080	34	17	Recombination
$H\alpha$	6562.819	6450-6700	6420-6450	6750–6790	2	7	Recombination

Note. Column (1): BEL name. Column (2): BEL wavelength. Column (3): BEL integration windows. Column (4): Left continuum windows. Column (5): Right continuum windows. Column (6): number of CL AGNs found in DESI. Column (7): number of CL candidates found in DESI. Column (8): physical mechanism of the BEL.

searching for CL AGNs and candidates in large sky surveys, as it helps to remove false-positive results and establish a reliable spectral variability definition.

3.3. Spectral Variability Definition (Selection Criteria)

Before defining the variability of the BEL, we require that the median signal-to-noise ratio (S/N) per pixel is at least greater than 1 for both the DESI and SDSS spectra. In previous studies (e.g., MacLeod et al. 2016; Yang et al. 2018; Graham et al. 2020; Green et al. 2022; Temple et al. 2023), a variety of criteria were chosen to describe the CL behavior of the BELs. Based on these previous studies, we adopt three spectrum parameters (N_{σ} , R, and $F_{\sigma, \text{dim}}$) to accurately describe the CL phenomenon.

 N_{σ} is defined as the significance in the variation of the BEL maximum flux and is a widely used definition applied for H β CL AGNs (MacLeod et al. 2019; Green et al. 2022), being the flux deviation between the dim spectrum and bright spectrum:

$$N_{\sigma} = (f_{\text{bright}} - f_{\text{dim}}) / \sqrt{\sigma_{\text{bright}}^2 + \sigma_{\text{dim}}^2}, \tag{1}$$

where f and σ are the spectral flux and variance, respectively, in erg cm⁻² s⁻¹ Å⁻¹. Green et al. (2022) smoothed the $N_{\sigma}(\text{H}\beta)$ array, subtracted the $N_{\sigma}(4750 \text{ Å})$ by the flux deviation array, and found the maximum relative value of $N'_{\sigma}(\text{H}\beta) = N_{\sigma}(\text{H}\beta) - N_{\sigma}(4750 \text{ Å})$. The AGNs with $N'_{\sigma}(\text{H}\beta) > 3$ are considered to be CL objects (see Green et al. 2022, Section 3.5, for details). Although this determination is effective at determining the "BEL disappeared or appeared" behavior, they also noticed that their selection criteria were very sensitive to minor BEL changes if the spectrum S/N was sufficiently high, which can be seen in several of the CL objects discovered in MacLeod et al. (2019) and Green et al. (2022).

In this paper, we aim to define a variability definition that can recreate our VI results and is also less biased by the S/N spectrum. We use the maximum value of the smoothed $N_{\sigma} > 3$ objects without the subtraction of $N_{\sigma}(4750\,\text{Å})$ as the first determination of the BEL variation, to limit the overall variation of both the continuum and BELs.

The second parameter (R) is defined as the ratio of the integrated BEL flux in the high-state spectrum to the integrated BEL flux in the low-state spectrum, which is used to constrain the total flux change of the BELs. As mentioned and inspired by MacLeod et al. (2019), we further adopt the R value to constrain the overall BEL flux change, which is defined as:

$$R = (F_{\text{bright}} - F_{\text{dim}}) / F_{\text{dim}}, \tag{2}$$

where F_{bright} or F_{dim} is the BEL total flux. Integration and spectral fitting are two widely used tools to obtain the BEL flux in the field of reverberation mapping (Peterson 1993; Hu et al. 2020). The integration method used in this work provides a quick and easy way to measure the BEL flux, which is suitable for the massive AGN data set released by DESI. We note that the accuracy of the integration may be affected by the host contribution or optical (or UV) Fe II lines. By subtracting the continuum as a straight line defined by two continuum windows, the BEL flux is measured by a simple integration method (see the details in Figure 2 of Hu et al. 2020). The BEL integration windows are carefully adjusted to ensure the best match with the first stage of the VI results. The information on the integration windows is listed in Table 3.

If we assume that the [O III] flux is unchanged, the R value we use is the same as the criterion defined in Winkler (1992):

$$R = \frac{F_{\text{bright,H}\beta}/F_{\text{bright,[O III]}}}{F_{\text{dim,H}\beta}/F_{\text{dim,[O III]}}} - 1.$$
 (3)

An AGN would be classified as different subtypes if the H β and [O III] flux ratio change were larger than 1.5, such as from Type 1.2 to Type 1.5 or from Type 1.5 to Type 1.8 (see the definition in Winkler 1992 for details), which we would refer to as a CL candidate in our sample. Based on H β , we adopt R > 1.5 as the CL candidate selection criterion for all BELs.

The last parameter $F_{\sigma,\text{dim}}$ represents the significance of the weak BEL, which is calculated from the dim spectrum:³⁹

$$F_{\sigma, \text{dim}} = \sum f_{\text{dim}} / \sqrt{\sum \sigma_{\text{dim}}^2}.$$
 (4)

Since the narrow-component emission lines (such as narrow $H\beta$ and [NII]) could exist in the dim spectra to increase the $F_{\sigma, \text{dim}}$ value, we take a different $F_{\sigma, \text{dim}}$ value for Balmer lines and other lines. Another reason for the lower $F_{\sigma, \text{dim}}$ value for the other lines is mainly due to the lower S/N for high-redshift AGNs.

When the S/N is high enough, the AGNs with a tiny broad component may be categorized as CL candidates. Compared with the weak component, we care more about the flux variation ratio. Thus, in the case of R > 1.5, we restrict $F_{\sigma, \dim} < 5$ for Balmer lines ($F_{\sigma, \dim} < 3$ for the other lines) as the criterion for CL AGNs. As R increases, we lower the limit

³⁹ For a turn-on CL AGN, the SDSS spectrum is at the dim state. If a CL AGN is marked as a turn-off, the dim spectrum will be from DESI.

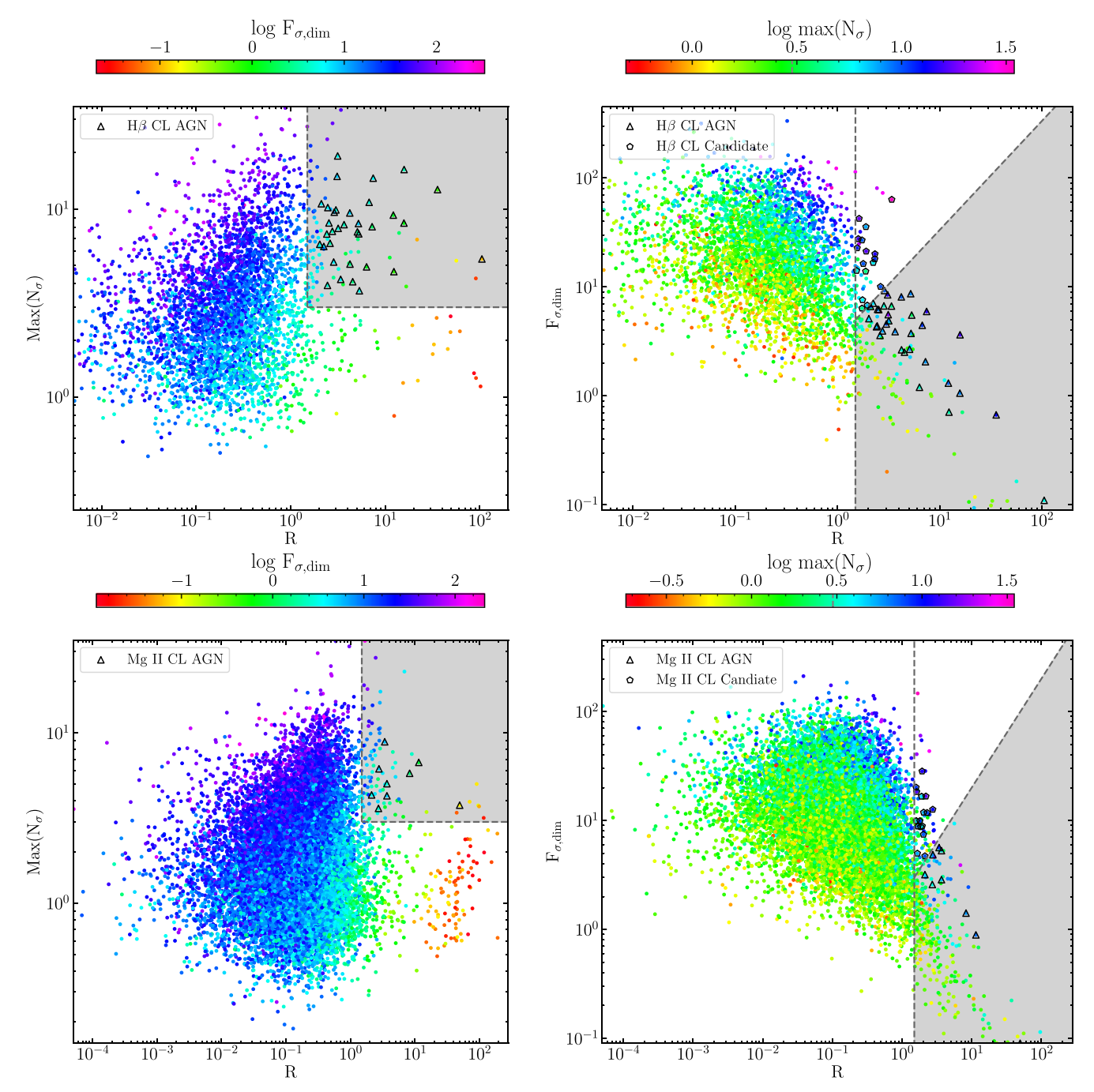


Figure 2. Distribution of CL AGNs in parameter spaces of $Max(N_{\sigma})$ vs. R (left panel) and parameter spaces of R vs. $F_{\sigma,dim}$ (right panel). The solid scatters represent the measurements of all AGN parameters (the H β or Mg II lines in the spectrum). The hollow triangles and pentagons represent the final CL AGNs and CL candidates after the second stage of VI. The gray shading shows the parameter thresholds for CL AGNs. The dashed gray lines are the corresponding boundaries.

of $F_{\sigma, \text{dim}}$ and use a straight line to divide CL AGNs and candidates with $F_{\sigma, \text{dim}} = 3.33R$ for Balmer lines or $F_{\sigma, \text{dim}} = 2.0R$ for the other lines, as plotted in Figure 2.

By combining these three parameters, we can accurately describe the CL behavior of the BELs. As mentioned before, our CL AGNs are mainly for the transition between type 1.x to type 1.9, while the CL candidates are mainly an intermediate transition, similar to those from type 1.2 (1.5) to 1.5 (1.8) for H β . The final variability definitions of these parameter thresholds are also established based on the results from the VI check and the comparison with previous studies. The final selection criteria for CL candidates and AGNs are:

- 1. CL candidates: $Max(N_{\sigma}) > 3$, R > 1.5;
- 2. CL AGNs for H α and H β : Max(N_{σ}) > 3, R > 1.5, $F_{\sigma, \text{dim}}$ < 3.33R; and
- 3. CL AGNs for Mg II, C III], and C IV: Max(N_{σ}) > 3, R > 1.5, $F_{\sigma, \text{dim}} < 2.0R$.

It is important to keep in mind that these parameter thresholds are tentative and may need to be refined or adjusted based on future large data sets. This selection method is expected to be less biased by the spectral S/N and provide a robust and efficient way to identify CL AGNs in the DESI project. We also note that spectral decomposition may result in identifying weak broad components, even though the BELs disappeared in

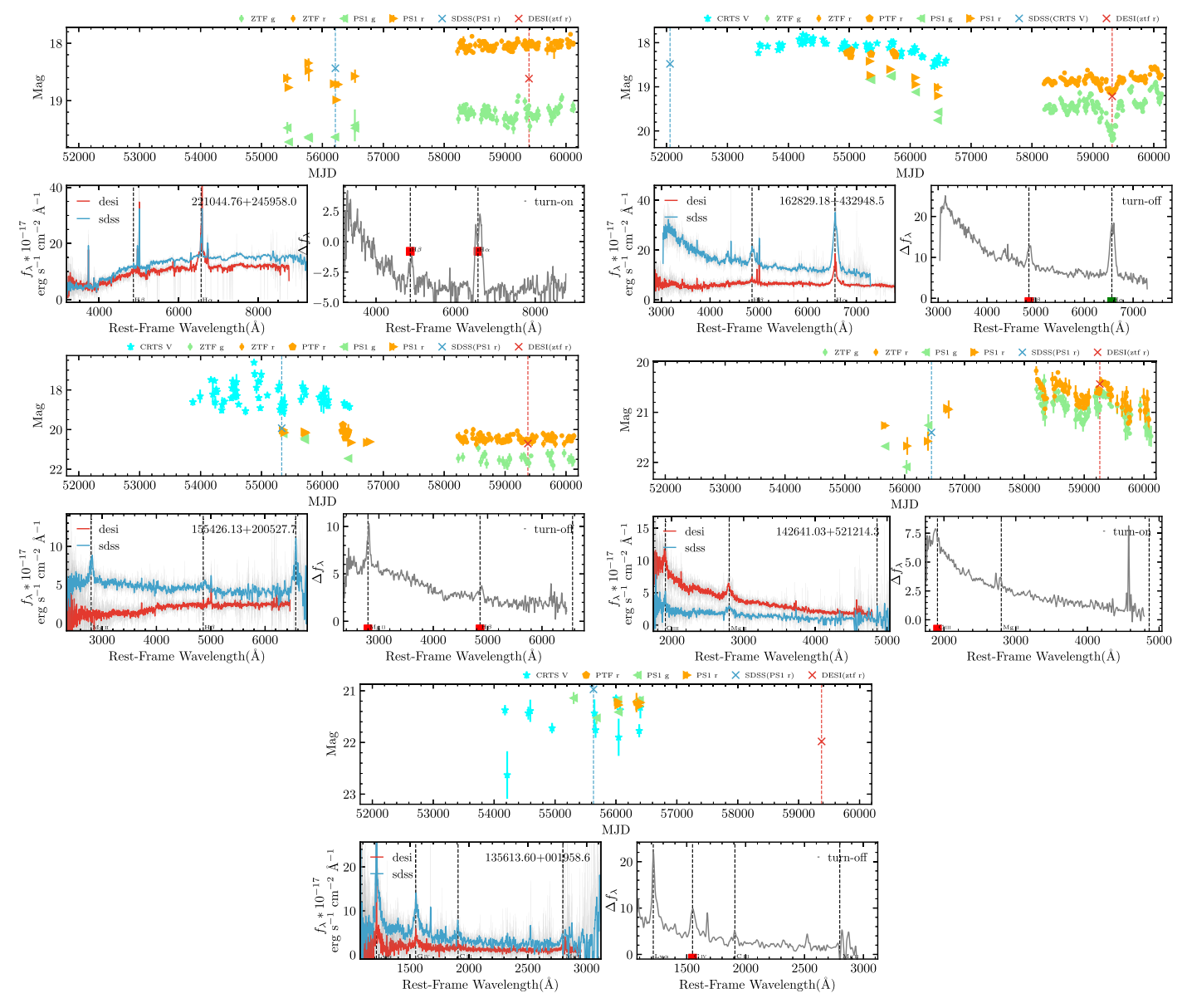


Figure 3. Five CL AGN example spectra of $H\alpha$ (top left), $H\beta$ (top right), Mg II (middle left), C III] (middle right), and C IV (bottom) found in DESI. In each figure, the top panel displays the spectral pseudophotometry with red (blue) "x" markers for DESI (SDSS) and the light curves from CRTS (stars), PS1 (triangles), PTF (pentagons), and ZTF (dots) when available. The bottom left panel shows the smoothed SDSS and DESI spectra, represented by the blue and red lines, respectively (the shaded region corresponds to the original spectrum). The spectra are derived from survey pipelines and have been corrected for galactic extinction and shifted to the rest frame (without [O III]-based calibration). Note that the DESI spectrum covers less flux from the host galaxy than SDSS in 221044.76+245958.0 (Figure 4). The gray line in the lower right panel represents the difference between the two spectra, obtained by subtracting the dim spectrum from the bright one. The black dashed vertical lines indicate the presence of $H\alpha$, $H\beta$, Mg II, C IV, and $Ly\alpha$ lines. The red and green blocks represent the CL line features and candidate features, respectively.

the VI results. Therefore, regardless of whether the BEL is disappearing or not, CL candidates and CL AGNs may be incorrectly identified due to the coincidence of spectral sampling or weak BEL flux covered by the host galaxy (this will be discussed in Section 4.3).

In Figure 2, you can see there is a clear correlation between these three parameters, revealed by plotting two parameters and color-coding the third. The population of AGNs does show a continuum of these parameters, with the CL AGNs at the most extreme end of the distribution. However, these plots make it clear that the most important parameter for distinguishing CL AGNs is the *R* parameter, with CL AGNs sitting in a very sparsely populated region of *R* values. The log scale in these plots shows that the *R* values of CL AGNs are typically orders

of magnitude higher than most AGNs. On the other hand, CL AGNs are in the same $Max(N_{\sigma})$ range as about one-third of the AGNs in our sample and they are in the same $F_{\sigma, \text{dim}}$ range as about one-fifth of the sample.

3.4. Flux Calibration Check

Several previous studies carried out a further flux calibration based on either an [O III] (5007 Å) calibration or using a photometric light curve to exclude fiber position and/or aperture issues introduced from the program selection (Yang et al. 2018; MacLeod et al. 2019; Green et al. 2022). In this work, we combine both methods to further check the selected CL AGNs.

Table 4 Sample Properties for the CL AGNs Presented in This Study

Object Name (1)	R.A.	Decl.	Redshift	g (mag)	r (mag) (6)	z (mag)	MJD_1	MJD_2	N_{σ} (10)	R (11)	$F_{\sigma, \text{dim}}$ (12)	Transition (13)	Line (14)
* /	(2)	(3)	(4)	(5)		(7)	(8)	(9)	`		`_	`	
075448.10+345828.5	118.7004	34.9746	0.7311	21.49	21.50	20.92	55488	59226	5.22	2.85	6.70	Turn-off	Нβ
085913.72+323050.8	134.8072	32.5141	1.1217	20.48	20.18	20.35	52989	59226	7.89	3.32	3.41	Turn-on	C III]
95035.55+321601.0	147.6482	32.2670	1.7181	20.59	20.54	20.33	56325	59280	4.40	2.24	4.46	Turn-on	C III]
									4.32	2.13	3.18	Turn-on	Mg II
03818.29+332437.2	159.5762	33.4103	1.2028	21.10	20.65	20.63	58497	59224	3.93	2.40	3.19	Turn-on	C III]
13737.38+511839.9	174.4058	51.3111	1.0671	20.70	20.48	20.39	56416	59307	4.34	2.68	1.51	Turn-off	C III]
15103.77+530140.6	177.7657	53.0280	0.5475	22.22	21.83	20.78	57423	59307	3.76	49.49	0.09	Turn-off	Mg II
									8.05	7.27	2.06	Turn-off	$H\beta$
15210.24+520205.1	178.0427	52.0347	0.6179	21.33	21.36	20.97	56416	59307	4.10	4.53	2.52	Turn-on	$H\beta$
15403.00+003154.0	178.5125	0.5317	0.4484	21.10	20.21	19.44	51943	59312	4.92	6.35	1.20	Turn-off	$H\beta$
									5.79	8.28	1.41	Turn-off	Mg II
21033.30-011755.6*	182.6388	-1.2988	0.5434	20.03	20.04	19.49	52367	59314	14.60	7.46	5.96	Turn-off	$H\beta$
22319.70+312737.0	185.8321	31.4603	1.5188	21.89	21.54	21.24	58488	59291	3.60	2.72	2.58	Turn-on	Mg II
25545.34+232348.0	193.9390	23.3967	0.5096	21.18	21.20	20.51	56312	59338	3.92	2.45	4.39	Turn-off	$H\beta$
25610.42+260103.4	194.0434	26.0176	1.1957	20.57	19.89	19.94	54505	59337	3.81	4.80	2.34	Turn-on	C III]
33044.43+072628.8	202.6851	7.4413	0.4634	19.48	19.44	19.11	53556	59370	6.15	2.77	4.84	Turn-off	Mg II
									7.89	3.18	4.90	Turn-off	Цβ
33344.70+335622.7	203.4363	33.9396	1.1452	21.50	21.12	21.30	58492	59292	4.38	3.09	2.82	Turn-on	C III] Hβ Mg II C IV Mg II
34037.05+131819.2	205.1544	13.3054	0.3478	20.78	19.82	19.08	53858	59372	7.61	2.76	3.95	Turn-off	$H\beta$
34554.00+084537.3	206.4750	8.7603	0.6020	20.76	20.37	20.21	55973	59371	4.27	3.68	5.28	Turn-on	Mg II
35613.60+001958.6	209.0567	0.3330	2.3286	21.62	21.45	21.21	55631	59376	4.19	2.58	4.89	Turn-off	C IV
35624.58+350813.1	209.1025	35.1370	0.7983	22.18	21.66	20.74	55268	59350	5.03	3.68	2.86	Turn-off	Мяп
35801.62+115331.8	209.5068	11.8922	0.2667	20.60	19.68	19.14	53144	59378	10.86	6.76	4.45	Turn-off	Нβ
40659.07+032601.9	211.7461	3.4339	0.5995	19.94	19.86	19.57	52045	59377	6.32	2.24	7.09	Turn-off	Нβ
40957.72-012850.5	212.4905	-1.4807	0.1352	19.05	18.21	17.49	55383	59338	10.18	2.47	6.23	Turn-off	Нβ
41535.46+022338.7	213.8977	2.3941	0.3519	20.50	19.49	18.60	51994	59370	16.25	9.36	14.27	Turn-off	$H\alpha$
+1333.40 022330.7	213.0711	2.3741	0.5517	20.30	17.47	10.00	31//-	37310	16.23	15.84	3.64	Turn-off	Нβ
41801.50+525200.7	214.5063	52.8669	1.1555	21.98	21.50	21.02	56755	59314	3.27	5.63	1.82	Turn-off	C III]
41923.44-030458.7	214.8477	-3.0830	2.6846	20.47	20.39	20.34	55333	59368	4.52	3.18	1.94	Turn-on	C III]
42641.03+521214.3	216.6710	52.2040	1.0493	21.48	21.19	20.94	56448	59260	3.70	70.89	0.04	Turn-on	C III]
44003.98+061936.5	220.0166	6.3268	0.5395	19.44	19.31	18.96	55684	59377	8.43	2.54	6.20	Turn-on	Нβ
44051.17+024415.8	220.2132	2.7377	0.3963	20.09	19.31	19.10	55620	59377	7.56	5.08	2.68	Turn-off	$H\beta$
45913.90+360051.4	224.8079	36.0143	0.5526	20.09	20.10	20.08	53121	59351	8.26	3.67	3.89	Turn-on	$H\beta$
52517.57+401357.6	231.3232	40.2327	0.3320	19.99	19.77	19.24	58175	59354	7.38	5.25	3.75	Turn-off	$H\beta$
52517.37+401337.0 52551.37+184552.0	231.4640	18.7645		19.59	18.84	19.24	54328	59370	8.42	15.78	1.06	Turn-off	$H\beta$
	232.2865	8.5343	0.4360 2.6581		20.76		56002			4.29			,
52908.75+083203.5 53140.04+373755.4				21.03		20.57		59366	4.55		1.91	Turn-on	C III]
53149.94+372755.4	232.9581 234.3101	37.4654 45.7299	0.9951 0.4688	20.94	20.85 20.24	20.81	58230 52781	59351 59385	3.76	1.92 3.40	3.37 5.64	Turn-off	C III]
53714.41+454347.7	234.3101	45.7299	0.4688	21.09	20.24	19.28	32/81	39383	8.87			Turn-off	Mg II
52020 02 + 272052 C	224 0122	27 (492	1 4107	22.57	21.00	21.01	50050	50275	9.28	12.18	1.31	Turn-off	Hβ
53938.92+373853.8	234.9122	37.6483	1.4187	22.57	21.90	21.91	58258	59375	3.71	2.16	3.74	Turn-on	C III]
54742.72+012541.0	236.9280	1.4281	0.6879	19.86	19.88	19.66	55359	59352	14.93	3.10	8.47	Turn-on	Нβ
55426.13+200527.7	238.6089	20.0910	0.5215	22.21	20.94	20.09	55332	59374	6.71	11.48	0.89	Turn-off	Mg II
									5.42	105.42	0.11	Turn-off	$H\beta$
60047.63+331310.7	240.1985	33.2196	0.3608	20.01	19.35	18.59	53142	59358	10.67	2.11	6.63	Turn-off	$H\beta$
60139.10+412529.3	240.4130	41.4248	0.4645	21.35	20.56	19.58	52824	59354	9.89	3.01	4.57	Turn-off	$H\beta$
160310.99+432928.9	240.7958	43.4914	0.4923	20.33	20.03	19.35	52756	59321	8.37	5.21	8.68	Turn-off	$H\beta$
160337.12+242513.9	240.9047	24.4205	0.7058	22.13	22.14	21.17	55327	59376	9.62	2.89	9.28	Turn-off	$H\beta$

Table 4 (Continued)

Object Name (1)	R.A. (2)	Decl. (3)	Redshift (4)	g (mag) (5)	r (mag) (6)	z (mag) (7)	MJD ₁ (8)	MJD ₂ (9)	N_{σ} (10)	R (11)	$F_{\sigma, \mathrm{dim}}$ (12)	Transition (13)	Line (14)
160730.20+560305.5	241.8759	56.0515	0.7172	21.62	21.35	20.70	56430	59311	6.57	2.61	3.59	Turn-on	Нβ
161542.41+233143.9	243.9267	23.5289	0.5757	20.48	20.10	19.67	55331	59376	7.36	2.41	4.31	Turn-off	$H\beta$
161903.04+540529.0	244.7627	54.0914	0.6033	20.76	20.78	20.43	58248	59311	5.09	4.24	2.65	Turn-on	$H\beta$
162106.25+371950.7	245.2761	37.3307	1.3883	21.28	20.89	20.96	58247	59350	3.84	1.83	2.16	Turn-off	C III]
162829.18+432948.5*	247.1216	43.4968	0.2599	19.80	19.22	18.73	52057	59316	9.53	4.22	8.11	Turn-off	$H\beta$
164331.90+304835.5	250.8830	30.8099	0.1837	19.71	18.75	18.09	52793	59386	12.69	35.76	0.67	Turn-off	$H\beta$
164709.87+532202.2	251.7911	53.3673	1.2008	21.45	21.03	20.93	57190	59383	7.06	3.72	4.89	Turn-on	C III]
164725.15+351754.3	251.8548	35.2985	0.6886	20.95	20.91	20.82	55828	59312	4.64	12.35	0.71	Turn-on	$H\beta$
164900.95+452016.8	252.2540	45.3380	0.5806	20.50	20.48	20.18	58021	59354	6.49	2.03	5.12	Turn-on	$H\beta$
213135.84+001517.0	322.8994	0.2547	2.4755	21.68	21.39	20.79	55450	59382	4.95	3.07	2.59	Turn-on	C III]
213400.68+013828.4	323.5029	1.6412	0.9973	20.87	20.61	20.52	58040	59380	4.20	20.09	0.56	Turn-on	C III]
213628.50-003811.8	324.1188	-0.6366	2.2368	21.94	22.02	21.34	55450	59382	4.89	4.17	2.35	Turn-off	C III]
221044.76+245958.0	332.6865	24.9995	0.1199	20.14	19.02	18.19	56213	59392	3.67	5.33	5.52	Turn-on	$H\beta$
									3.05	1.82	55.05	Turn-on	$H\alpha$
221925.57+272806.4	334.8566	27.4685	0.2282	20.60	19.58	18.84	57575	59392	19.17	3.14	5.57	Turn-off	$H\beta$
223440.56+272437.9	338.6690	27.4105	1.0203	21.00	20.72	20.68	57654	59403	4.03	7.81	0.66	Turn-on	C III]
224657.70-003242.5	341.7404	-0.5451	0.4157	20.43	19.75	18.98	52590	59404	4.22	3.38	6.68	Turn-on	$H\beta$

Notes. Column: (1) name. Column (2): R.A. Column (3): decl. Column (4): redshift. Column (5): photometric magnitude for g band. Column (6): photometric magnitude for g band. Column (6): photometric magnitude for g band. Column (8): MJD for SDSS spectrum. Column (9): MJD for DESI spectrum. Column (10): Flux deviation from Equation (1). Column (11): flux change ratio from Equation (2). Column (12): the significance of the BEL. Column (13): CL type. Column (14): target BEL. We note that the three targets with asterisks have been replicated from other studies. (121033.30-011755.6 refers to MacLeod et al. 2019, while 162829.18 +432948.5 refers to Zeltyn et al. 2022).

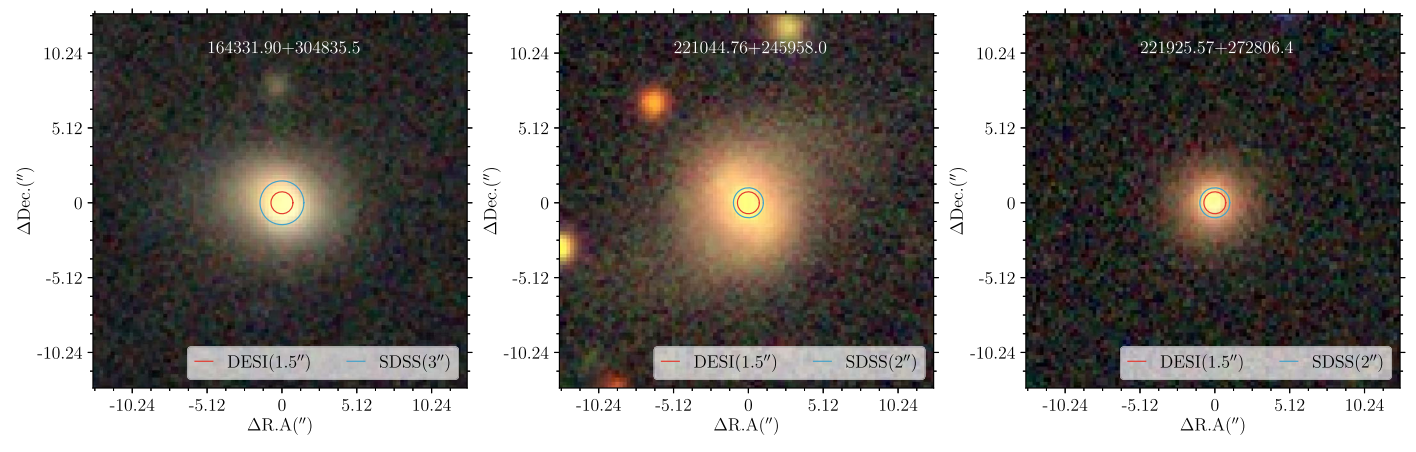


Figure 4. The DESI Legacy images for J164331.90+304835.5 (left), J221044.76+245958.0 (middle), and J221925.57+272806.4 (right). The blue and red circles represent the fiber diameters of SDSS and DESI.

The [O III] flux should remain relatively unchanged, since the [O III] emission line probes the region reaching hundreds of parsecs to several kiloparsecs away from the central ionization source and originates from the narrow-line region and host galaxy even though there are still some controversies about the [O III] flux variation (Barth & Bentz 2016; Zhang & Feng 2016; Yan et al. 2019). If the [O III] flux difference between the two spectra is less than 15%, the possible reasons are fiber diameter differences, changes in the observation seeing, and possible flux changes, in which case the recalibration of the spectrum will cause a fake CL phenomenon. Therefore, we adopted the [O III] calibration for those [O III] luminosities that changed between the DESI and SDSS spectra beyond the 15% deviation. We remove those objects that do not satisfy the criteria outlined in Section 3.3 after calibration to ensure the accuracy of our sample.

To align the resolution of the DESI and SDSS spectra, we employ a Gaussian kernel to convolve the DESI spectra ($R \sim 4000$) to match the lower resolution of the SDSS spectra ($R \sim 2000$). Following the approach outlined in Du et al. (2018), we conduct an [O III]-based calibration to scale the flux of the SDSS spectrum, taking into account the [O III] flux ratio between DESI and SDSS for AGNs at $z \leqslant 0.75$.

However, considering that DESI has a smaller fiber diameter (1".5) than the SDSS fiber diameter (2".0), the extended O III] region (which can extend to more than 10 kpc) may all be outside of the fiber radius (Goddard et al. 2010). This would change the [O III] flux and can be exacerbated by variable seeing. Such an effect would be more significant at lower redshifts. In these cases, [O III] calibration may enlarge the flux of the emission line or continuum, thus we only use [O III] calibration to identify cases where the variation may be spurious and use the noncalibrated spectra in the final results shown in Figure 3.

The photometric light curve serves as a criterion for checking the presence of a flux calibration problem between the DESI and SDSS spectra. As mentioned in Guo et al. (2020), the SDSS spectrum may exhibit problematic spectral flux calibration, resulting in scatter of up to 20% at high redshift, known as fiber drop. This effect becomes more pronounced when screening for CL AGNs. Therefore, we utilized the publicly available light curves from CRTS, PTF, PS1, and ZTF to compare the relevant photometry with the pseudophotometry around the spectral modified Julian date (MJD). It is important

to note that the CRTS data were unfiltered at the time of observation and were subsequently converted to the V band, which may introduce inaccuracies in the pseudophotometry. Finally, 74 CL AGNs and 47 candidates were removed if their spectral photometry significantly deviated from the light curve, typically exceeding 0.5 mag.

Although the pseudophotometry for J164331.90+30483 5.5, J221044.76+245958.0, and J221925.57+272806.4 shows a deviation of approximately 0.5 mag compared to the ZTF light curve, we have decided to retain these objects, as they still meet our criteria after calibration based on [O III] measurements. Furthermore, since the redshift of these three objects is z < 0.25, the observed deviation is primarily attributed to inconsistencies in the contribution of starlight between the spectral diameter coverage and the ZTF point-spread-function-based photometric modeling. The DESI Legacy images confirm the presence of significant extended source features in their host galaxies, as shown in Figure 4. It is worth noting that the DESI and SDSS fiber diameters capture less starlight from the host galaxy compared to the ZTF light curve.

After conducting [O III]-based calibration and analyzing the photometric light curve, we have removed 73 CL AGNs (38 candidates) from the original sample of 130 CL AGNs (91 candidates). Among these, two CL AGNs were identified as having DESI flux calibration problems. Figure 5 illustrates the SDSS and DESI fiber drop effect.

4. Results

4.1. CL AGNs and Candidates

Within the current DESI project, we obtain 56 CL AGNs based on the variability definition outlined in Section 3.3 and the VI in Section 3.2, which are listed in Tables 1 and 2. Of these 56 AGNs, J162829.18+432948.5 was previously discovered in Zeltyn et al. (2022) and 121033.30-011755.6 was selected as a CL candidate reported by MacLeod et al. (2019) as having high optical variability, although spectra were lacking. Specifically, we identify 2 H α , 34 H β , 9 Mg II, 18 C III], and 1 C IV CL objects. While J221044.76+245958.0 is classified as a CL candidate in the selection criteria, we moved it from the CL candidates to CL AGNs with VI because the significance of its broad components was increased by narrow lines. Figure 3 shows five examples of H α , H β , Mg II, C III], and C IV CL AGNs, respectively, where the difference

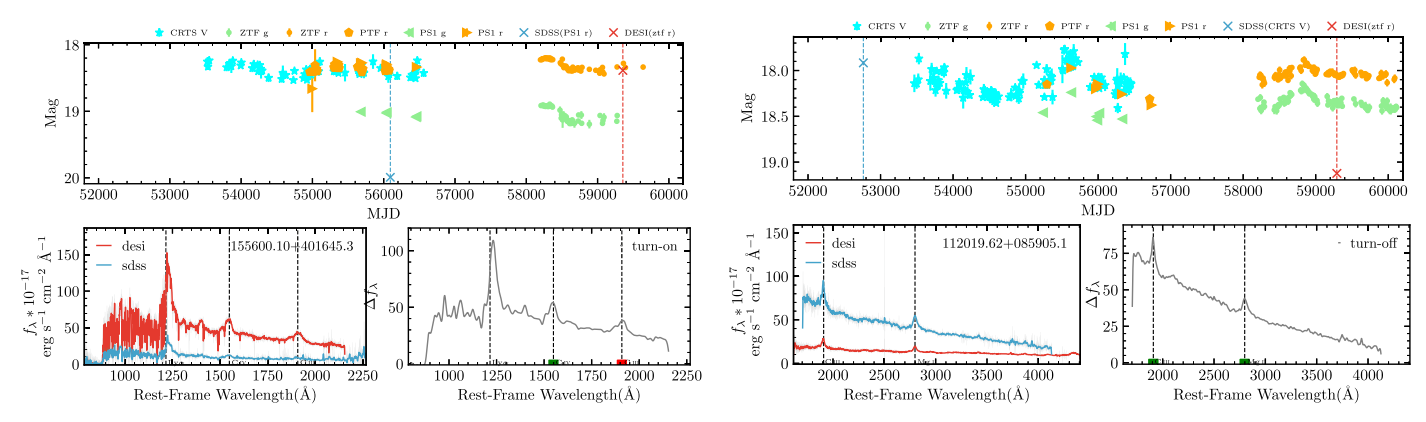


Figure 5. Two example spurious CL phenomena due to the SDSS (left) and DESI (right) flux calibration problem. The legends are same as in Figure 3. In the left (right) figure, the SDSS (DESI) spectrum does not match the calculated PS1 (ZTF) photometric magnitude ("x" markers) in the light curve, while the DESI (SDSS) spectrum aligns with the light curve. This suggests a discrepancy in flux calibration for this spectrum.

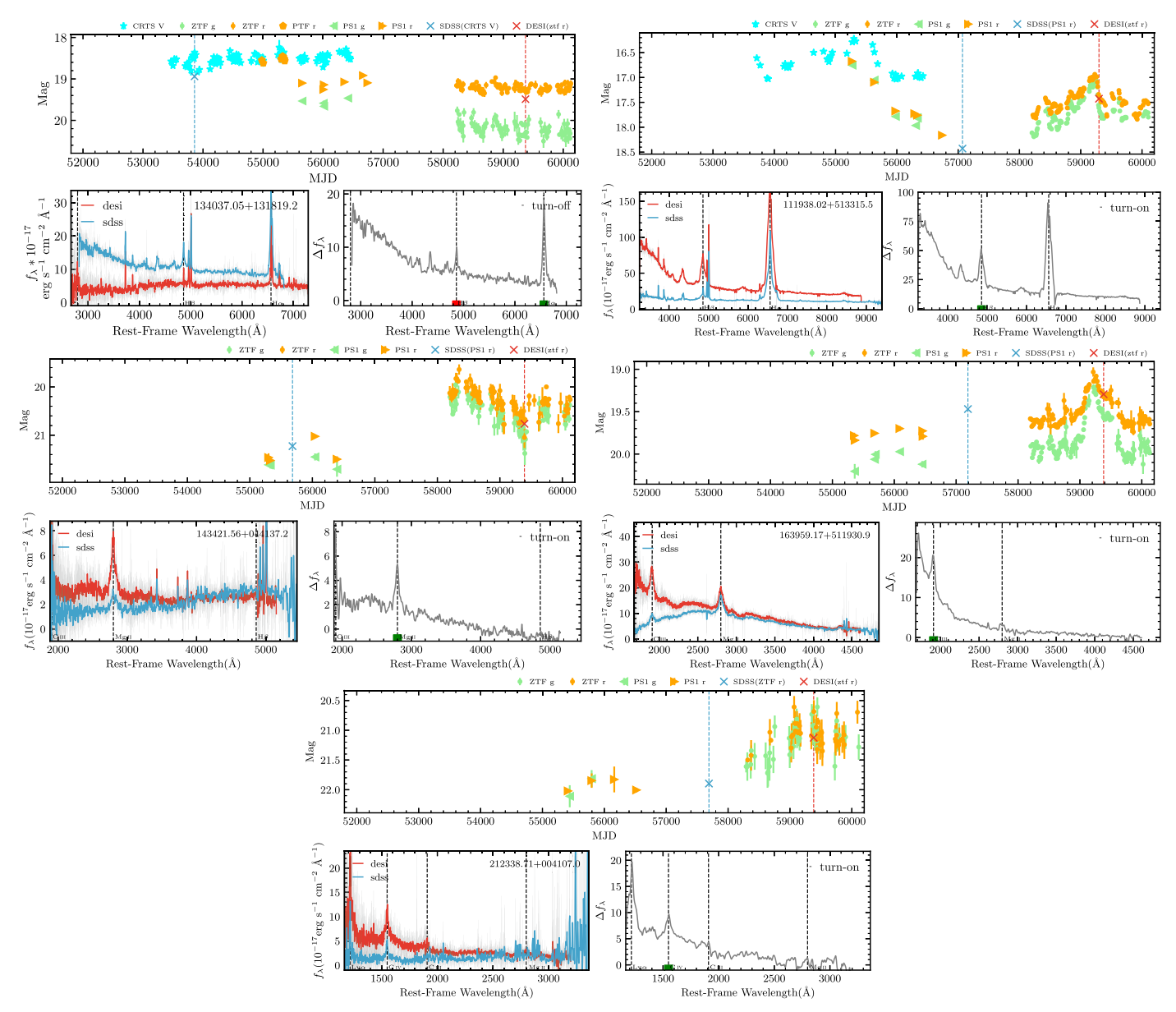


Figure 6. The same as Figure 3, but showing the CL candidates for $H\alpha$, $H\beta$, Mg II, C III], and C IV, respectively.

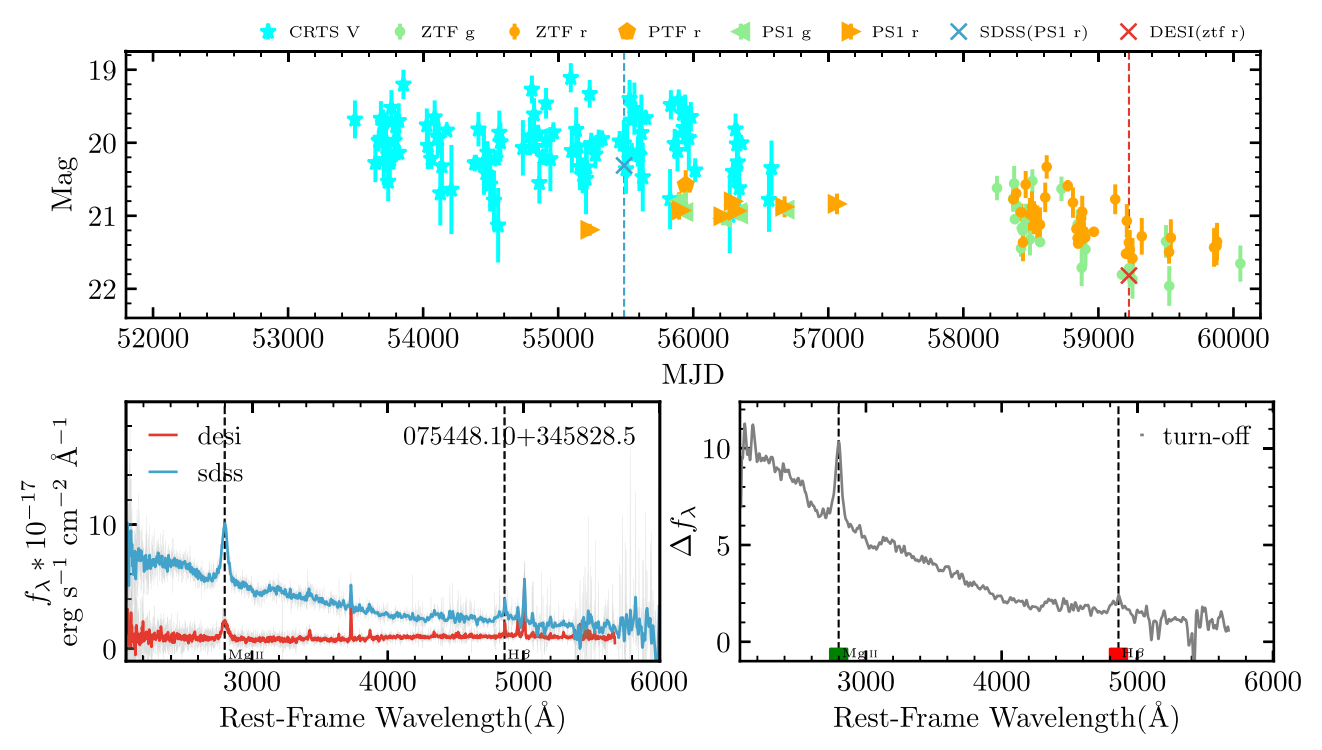


Figure 7. The rest of the CL AGNs. In each set, the top panels display the spectral pseudophotometry with red (blue) "x" markers for DESI (SDSS) and the light curves from CRTS (stars), PS1 (triangles), PTF (pentagons), and ZTF (dots) when available. The bottom left panel shows the smoothed SDSS and DESI spectra, represented by the blue and red lines, respectively (the shaded region corresponds to the original spectrum). The spectra are derived from survey pipelines and have been corrected for galactic extinction and shifted to the rest frame (without [O III]-based calibration). The gray line in the lower right panel represents the difference between the two spectra, obtained by subtracting the dim spectrum from the bright one. The black dashed vertical lines indicate the presence of H α , H β , Mg II, C III], C IV, and Ly α lines. The red and green blocks represent the CL line features and candidate features, respectively.

(The complete figure set (50 images) is available.)

Table 5
Sample Properties for the CL Candidate Features in Confirmed CL AGNs

Object Name (1)	R.A. (2)	Decl. (3)	Redshift (4)	g (mag) (5)	r (mag) (6)	z (mag) (7)	MJD ₁ (8)	MJD ₂ (9)	N_{σ} (10)	R (11)	$F_{\sigma, \text{dim}}$ (12)	Transition (13)	Line (14)
075448.10+345828.5	118.7004	34.9746	0.7311	21.49	21.50	20.92	55488	59226	14.52	2.20	16.65	Turn-off	Mg II
121033.30-011755.6	182.6388	-1.2988	0.5434	20.03	20.04	19.49	52367	59314	13.96	1.62	18.31	Turn-off	Mg II
134037.05+131819.2	205.1544	13.3054	0.3478	20.78	19.82	19.08	53858	59372	10.49	2.02	18.05	Turn-off	$H\alpha$
144051.17 + 024415.8	220.2132	2.7377	0.3963	20.09	19.77	19.10	55620	59379	9.47	1.61	14.16	Turn-off	$H\alpha$
152517.57+401357.6	231.3232	40.2327	0.3838	19.99	19.77	19.24	58175	59354	12.50	2.61	31.46	Turn-off	$H\alpha$
									7.87	2.29	11.76	Turn-off	Mg II
160139.10+412529.3	240.4130	41.4248	0.4645	21.35	20.56	19.58	52824	59354	10.53	2.76	12.60	Turn-off	Mg II
160310.99+432928.9	240.7958	43.4914	0.4923	20.33	20.03	19.35	52756	59321	8.42	1.59	20.09	Turn-off	Mg II
162829.18+432948.5	247.1216	43.4968	0.2599	19.80	19.22	18.73	52057	59316	13.43	1.93	63.19	Turn-off	$H\alpha$
164331.90+304835.5	250.8830	30.8099	0.1837	19.71	18.75	18.09	52793	59386	25.42	1.81	73.12	Turn-off	$\mathrm{H}\alpha$

Note. The columns are the same as in Table 4.

spectrum is the subtraction of the dim spectrum from the bright spectrum. Table 4 summarizes the properties of the 57 CL AGNs.

To further study the whole process of CL AGNs, we also search for CL AGN candidates that are in the process of changing or about to happen. In the 56 CL AGNs we have discovered, nine AGNs have candidate additional BEL variations (listed in Table 5). We also provide another 44 CL candidates for five BELs, as shown in Table 6. The whole CL candidate sample contains 53 AGNs, including $7~{\rm H}\alpha$, $17~{\rm H}\beta$, $16~{\rm Mg~II}$, $10~{\rm C~III}$], and $5~{\rm C~IV}$ CL candidates. To highlight the

difference between the confirmed CL AGNs and the candidates, Figure 6 provides five selected examples of CL candidate spectra. Figure 7 shows the remaining 50 CL AGNs.

4.2. Timescale and Transition State

In Figure 8, we plot the timescales of both the 56 confirmed CL AGNs and the 44 CL candidates between the two observations in the observed frame and rest frame. We note that the CL AGNs that show different BEL behavior from the same source are counted repeatedly. For instance, a case with varying $H\beta$ and Mg II will be included once in the Mg II sample

Table 6Sample Properties for the CL AGN Candidates Presented in This Study

Object Name (1)	R.A. (2)	Decl. (3)	Redshift (4)	g (mag) (5)	r (mag) (6)	z (mag) (7)	MJD ₁ (8)	MJD ₂ (9)	N_{σ} (10)	R (11)	$F_{\sigma, \text{dim}}$ (12)	Transition (13)	Line (14)
091452.90+323347.1	138.7204	32.5631	1.5782	20.99	20.88	20.63	54550	59251	6.89	1.73	5.54	Turn-on	C III]
102012.84+324737.2	155.0535	32.7937	0.6200	20.20	20.13	19.82	53442	59218	7.59	1.90	35.65	Turn-off	$H\beta$
102104.98+440355.5	155.2708	44.0654	0.6046	20.12	20.06	19.70	57419	59218	4.13	1.74	6.37	Turn-on	$H\beta$
111634.91+540138.8	169.1455	54.0274	1.0618	21.44	20.90	20.73	57135	59307	5.49	1.66	4.98	Turn-off	Mg II
111938.02+513315.5	169.9084	51.5543	0.1071	18.35	18.46	17.91	57071	59298	33.71	3.40	63.43	Turn-on	$H\beta$
112634.33+511554.5	171.6431	51.2652	1.5319	20.97	20.62	20.82	57071	59308	5.24	2.25	5.17	Turn-on	C III]
120332.06+563100.3	180.8836	56.5168	1.5200	21.16	20.31	20.35	56429	59309	4.36	1.64	6.91	Turn-on	C III]
123557.86+582122.9	188.9911	58.3564	0.2116	19.39	18.79	18.47	52790	59298	9.68	1.74	26.90	Turn-off	$H\beta$
124446.47+591510.8	191.1936	59.2530	0.6836	20.90	20.98	20.52	56443	59308	7.35	2.03	7.43	Turn-off	Mg II
124931.53+364816.4	192.3814	36.8045	1.4279	20.73	20.26	20.43	57481	59351	6.08	1.64	7.68	Turn-on	C III]
									9.16	1.80	9.89	Turn-on	Mg II
125646.90 + 233854.8	194.1954	23.6486	0.8159	20.45	20.54	20.23	54212	59338	11.70	1.94	28.28	Turn-off	Mg II
140337.55 + 043126.2	210.9065	4.5239	0.5378	19.79	19.77	19.85	52045	59312	11.43	2.32	18.06	Turn-off	$H\beta$
141735.11 + 043954.6	214.3963	4.6652	0.4371	21.38	20.61	19.82	55654	59369	3.92	1.67	6.39	Turn-on	$H\alpha$
141841.39 + 333245.8	214.6725	33.5460	0.5890	22.10	21.58	20.50	55280	59292	6.05	1.76	7.60	Turn-on	$H\beta$
142118.41 + 505945.2	215.3268	50.9959	1.0279	19.87	19.62	19.77	56415	59312	10.19	2.59	8.54	Turn-off	C III]
143421.56+044137.2	218.5899	4.6937	0.9070	21.17	20.96	20.11	55682	59393	5.20	2.04	11.84	Turn-on	Mg II
143528.95 + 134705.7	218.8706	13.7849	0.7701	20.47	20.53	20.01	56014	59292	9.79	1.79	16.35	Turn-off	$H\beta$
144813.63 + 080734.2	222.0568	8.1262	0.4414	18.79	18.74	18.50	54555	59379	14.48	2.33	20.10	Turn-on	$H\beta$
150232.97 + 062337.6	225.6374	6.3938	0.6430	19.79	19.88	19.51	55712	59377	7.03	1.96	6.78	Turn-on	$H\beta$
150754.87 + 274718.7	226.9786	27.7885	3.3013	21.46	20.93	20.94	55365	59379	4.57	1.76	4.03	Turn-on	C IV
151859.62+061840.5	229.7484	6.3112	0.5505	21.15	20.70	20.01	55710	59368	7.11	1.70	8.83	Turn-off	Mg II
152425.40+232814.7	231.1058	23.4707	0.6524	21.90	22.00	21.63	55680	59369	4.33	1.91	16.60	Turn-on	Mg II
153644.03+330721.1	234.1835	33.1225	0.7503	20.02	19.91	19.77	53149	59309	7.76	2.13	4.71	Turn-on	Mg II
153920.83 + 020857.2	234.8368	2.1493	0.3114	18.99	18.79	18.23	54562	59369	16.76	1.91	21.26	Turn-off	$H\beta$
153952.21 + 334930.8	234.9676	33.8252	0.3289	18.25	18.06	17.57	52823	59309	15.87	1.60	27.67	Turn-on	$H\beta$
154025.23+211445.6	235.1052	21.2460	0.3907	19.51	19.19	18.79	54232	59376	18.09	1.63	42.45	Turn-off	$H\beta$
155732.71+402546.3	239.3863	40.4295	1.0899	20.64	20.40	20.52	58280	59354	3.73	1.67	7.21	Turn-on	C III]
160129.75+401959.5	240.3740	40.3332	1.5823	22.18	21.58	21.45	58280	59354	4.47	2.12	8.74	Turn-on	C IV
160451.29+553223.4	241.2137	55.5399	0.3127	20.92	19.70	18.93	57897	59321	5.21	1.54	14.11	Turn-on	$H\beta$
160712.23+151432.0	241.8010	15.2422	0.7789	21.58	21.16	20.67	55660	59292	4.08	1.89	13.91	Turn-off	$H\beta$
160808.47+093715.5	242.0353	9.6210	0.5624	21.58	20.72	19.60	54582	59368	4.43	1.60	9.91	Turn-off	Mg II
161235.23+053606.8	243.1468	5.6019	0.7869	22.21	21.73	20.45	55708	59353	4.80	1.85	8.73	Turn-on	Mg II
161812.85+294416.6	244.5536	29.7379	0.3125	20.29	19.68	18.94	52886	59358	13.03	2.18	36.64	Turn-off	$H\alpha$
163959.17+511930.9	249.9966	51.3252	1.1318	20.02	19.73	20.01	57190	59383	7.37	2.14	14.47	Turn-on	C III]
164621.95+393623.8	251.5915	39.6066	0.3448	18.86	18.73	18.25	52050	59379	11.75	1.56	22.80	Turn-off	$H\beta$
165919.33+304347.0	254.8306	30.7297	1.0375	20.26	19.79	19.82	58526	59356	6.46	2.36	7.33	Turn-on	C III]
170407.13+404747.1	256.0298	40.7964	1.2939	21.13	20.58	20.61	58281	59379	6.10	2.25	6.64	Turn-on	C III]
170624.94+423435.1	256.6039	42.5764	1.5936	21.25	20.91	20.78	58281	59379	10.55	2.03	32.09	Turn-on	CIV
172541.38+322937.8	261.4224	32.4938	0.6621	20.59	20.55	20.41	55721	59350	9.98	2.64	10.07	Turn-off	$H\beta$
205407.92+005400.9	313.5330	0.9003	1.6435	21.16	20.98	20.62	52914	59370	9.00	1.90	13.81	Turn-off	C III]
212216.44-014959.8	320.5685	-1.8333	0.1362	20.23	19.43	18.81	58039	59381	6.12	2.24	16.71	Turn-on	Нβ
212338.71+004107.0	320.9113	0.6853	2.0709	22.63	22.54	21.89	57691	59383	4.48	1.57	7.63	Turn-on	C IV
213430.72-003906.7	323.6280	-0.6519	1.8412	20.99	20.81	20.49	57693	59382	5.42	2.30	8.13	Turn-on	C IV
221932.80+251850.4	334.8867	25.3140	0.6264	22.10	21.37	20.40	56210	59403	3.83	1.95	8.88	Turn-off	Mg II

Note. The columns are the same as in Table 4

(green histogram) and once in the H β sample (blue histogram). Zeltyn et al. (2022) reported a timescale for the H β variation observed in J162829.18+432948.5 of only a few months (73 days), whereas we probe a timescale of up to 5643 days between the SDSS and DESI observations. The timescale represents the upper limit of the transition timescale and ranges from 330 to 5762 days. While the observed-frame histogram suggests that some differences may be attributed to a selection effect or observational bias, systematic differences between different samples persist. One reason may be due to the selection bias of a small sample size, which requires further investigation with a larger sample.

In our sample of 56 CL AGNs, 24 AGNs exhibit turn-on behavior, while 32 AGNs exhibit turn-off behavior, as listed in Table 4. The proportion of turn-offs and turn-ons for CL AGNs is consistent with previous work (MacLeod et al. 2016, 2019; Yang et al. 2018; Green et al. 2022). The redshift and magnitude distributions for turn-off and turn-on CL AGNs are shown in the bottom panels of Figure 1. Figure 9 shows the timescale for different emission lines with transition states, from which we can see that the turn-off timescales are larger than the turn-on timescales in all emission lines. However, due to the limited number of samples, whether there are different timescales for turn-on and turn-off CL AGNs still needs further, more complete sample verification.

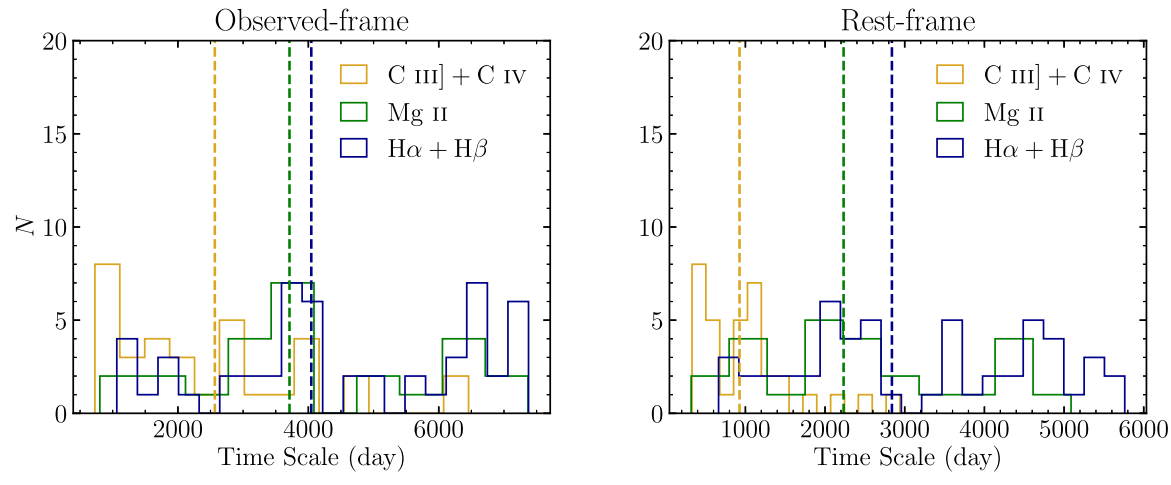


Figure 8. The histograms of the upper limits of the transition timescales for CL AGNs and CL candidates in observed frame (left panel) and rest frame (right panel). The dashed lines represent the median values of three samples. While it seems like C III] and C IV have lower rest-frame timescales than the other lines, the observed-frame histogram shows that that is partially due to a selection effect, since time dilation has made it impossible from our sample to detect carbon rest-frame lags longer than 3500 days.

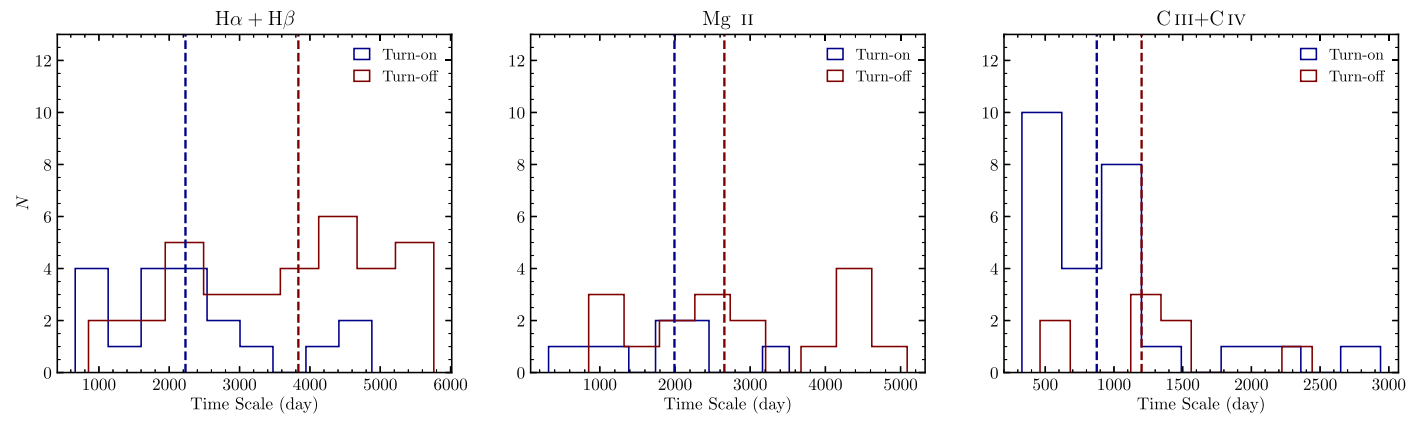


Figure 9. The histograms of the upper limits of the transition timescales for $H\alpha + H\beta$ (left panel), Mg II (middle panel), and C III] + C IV (right panel) CL AGNs and CL candidates in the rest frame (right panel). The dashed lines represent the median values of the samples.

4.3. Physical Origin

Despite the limitations on the information about the continuum luminosity and power-law index, it is evident that the majority of CL AGNs, from Figure 3, particularly for H α and H β , display the characteristic of being bluer when brighter (the optical and UV emission from the nucleus of an AGN becomes bluer when the overall brightness of the AGN increases), which is in line with many previous studies (LaMassa et al. 2015; MacLeod et al. 2016; Runnoe et al. 2016; Gezari et al. 2017; Yang et al. 2018; Graham et al. 2020; Green et al. 2022). From a quantitative standpoint, MacLeod et al. (2019) and Green et al. (2022) presented two separate CL AGN samples obtained through the method of spectral fitting, and both find a strong correlation between the change in H β flux and the variation in continuum flux (refer to Figure 3 in MacLeod et al. 2019 and Figure 8 in Green et al. 2022 for more details). This close relationship between the continuum and BEL variation suggests that the radiation from the accretion disk continues to drive the evolution of the BLR, even during the changing state. This phenomenon also implies that there is a rapid exchange of both material and energy occurring between the accretion disk and the BLR, indicating that the origin

of CL AGNs is more likely to come from changes in the accretion rate.

Despite this, there are still some uncertainties in the identification of CL AGNs. According to MacLeod et al. (2016) and Green et al. (2022), some CL AGNs exhibit backand-forth variability, where the weak $H\beta$ broad component disappears in one epoch, but reappears in another. This suggests that the discovery of CL AGNs is like a random sampling from a pool with constantly changing BELs.

One possible explanation for CL behavior is that the AGN is undergoing a transition from a low to high accretion rate state or vice versa. In the low-accretion-rate state, the emission from the central region is relatively weak, while in the high-accretion-rate state, the emission is much stronger. The transition between these two states can be triggered by various physical processes, such as the instability of the accretion disk or changes in the mass supply rate. Elitzur & Ho (2009) proposed that AGNs may have a critical luminosity that switches the BEL appearance and disappearance. This model is also supported by the discovered CL AGNs, which show a low accretion rate and low Eddington ratio (usually <0.1) in the dim spectrum. Given that the radiation regions of C III] and C IV are relatively small, another potential scenario that could

describe the C III] and C IV CL behavior is the association with an outflow.

Given that the majority of CL AGNs display the "bluer when brighter" trend, another potential explanation could be a change in the obscuration of the BLR, either due to dust clouds that move in and out of our line of sight or powerful winds that "blow out" the dust surrounding the nucleus. However, the former scenario has not been supported by polarization observations, timescale calculations, and mid-IR features for the majority CL AGNs (LaMassa et al. 2015; MacLeod et al. 2016; Sheng et al. 2017). Many of the turn-on CL AGNs exhibit a wavelength-dependent gain in continuum flux, appearing to change from a "red quasar" (e.g., Klindt et al. 2019; Fawcett et al. 2020) to a typical blue guasar (see Figure 3). This could indicate that dust is being removed from these systems, which may be evidence that these AGNs are undergoing a "blow-out" phase, in which powerful outflows clear out the surrounding gas/dust (Glikman et al. 2017; Fawcett et al. 2022; Stacey et al. 2022). Using spectroscopy over a 19 yr period, Yi et al. (2022) discovered a turn-on CL AGN that hosted powerful outflows, concluding that the quasar was shedding a surrounding dust cocoon, transitioning to a blue quasar. However, it is still unclear whether changes in the accretion disk could account for the change in continuum flux and also whether the difference in the dust extinction values over a 10-20 yr timescale is consistent with a blow-out phase. Several possible models have also been proposed to explain the CL phenomenon, including the cooling front model caused by a change in the magnetic field (Ross et al. 2020), the close binary black hole model (Wang & Bon 2020), and the magnetic-field-coupled accretion outflow model (Feng et al. 2021). In the picture of an advectiondominated accretion flow model, CL behavior might be caused by an intermittent accretion stream, which would result in a back-and-forth BEL pattern in the AGN (Noda & Done 2018). This study is a first step in an ongoing effort to constrain or test these models by analyzing a large sample of CL AGNs in the DESI project.

5. Conclusion

Using DESI early data, we carry out a systematic search for CL AGNs through crossmatching with the SDSS DR16 spectroscopic database. From a parent sample of 82,653 AGNs, the following points summarize our main findings:

- 1. We have compiled a sample of 56 CL AGNs selected based on VI and our defined criteria, which include 2 H α , 34 H β , 8 Mg II, 18 C III], and 1 C IV CL behaviors.
- 2. We find 10 candidate CL features in confirmed CL AGNs and provide another 44 CL AGN candidates, which show the dramatic flux variation of the emission lines, with a remaining significant broad component.
- 3. We identify 32 CL AGNs that display a turn-off transition and 24 CL AGNs that display a turn-on transition, whose timescales show significant differences, with the turn-offs larger than the turn-ons.
- 4. We confirm the tendency of bluer when brighter, which is consistent with the behavior of previously discovered CL AGNs.

Although our current research focuses on compiling a substantial sample of CL AGNs, future spectral decomposition work (such as a more accurate black hole mass and accretion

rate, as well as a detailed BEL measurement in the dim state) and dust extinction tests that will analyze the BELs and continuum could greatly enhance our understanding of the physical mechanisms behind CL activity (Fawcett et al. 2020, 2022). In addition, future studies of CL AGNs will be crucial in advancing our understanding of the growth and evolution of supermassive black holes and the properties of the circumnuclear material in AGNs (Ho 2005). The ongoing DESI project provides an exciting opportunity to gain further insights into the CL physical mechanism. In our follow-up work, we will attempt to verify the CL sequence and conduct further spectral decomposition to analyze the physical mechanism (MacLeod et al. 2016; Guo et al. 2019; Green et al. 2022). Additionally, we will continue to search for CL AGNs in DESI DR1 and investigate the differences and relationship between CL AGNs and normal AGNs.

Acknowledgments

We really appreciate the referee for useful and precious comments that significantly improved the manuscript. W.-J.G. would thank Suijian Xue, Luis C. Ho, and Jian-Min Wang for valuable discussions and comments. We also thank the DESI Publication Board Handler (Antonella Palmese) for providing timely help. This work is supported by the National Key R&D Program of China (grant No. 2022YFA1602902), the National Natural Science Foundation of China (NSFC; grant Nos. 12120101003, 12373010, and 11890691), and the Beijing Municipal Natural Science Foundation (grant No. 1222028). We acknowledge the science research grants from the China Manned Space Project with Nos. CMS-CSST-2021-A02 and CMS-CSST-2021-A04. V.A.F. acknowledges funding from a United Kingdom Research and Innovation grant (code: MRV0228301). M.S. acknowledges the Polish National Agency for Academic Exchange (Bekker grant BPN/BEK/ 2021/1/00298/DEC/1) and the European Union's Horizon 2020 Research and Innovation program under the Marie Skłodowska-Curie grant agreement (No. 754510).

This material is based upon work supported by the U.S. Department of Energy (DOE), Office of Science, Office of High-Energy Physics, under Contract No. DE-AC02-05CH11231, and by the National Energy Research Scientific Computing Center, a DOE Office of Science User Facility, under the same contract. Additional support for DESI was provided by the U.S. National Science Foundation (NSF), Division of Astronomical Sciences, under Contract No. AST-0950945 to the NSF's National Optical-Infrared Astronomy Research Laboratory; the Science and Technologies Facilities Council of the United Kingdom; the Gordon and Betty Moore Foundation; the Heising-Simons Foundation; the French Alternative Energies and Atomic Energy Commission (CEA); the National Council of Science and Technology of Mexico (CONACYT); the Ministry of Science and Innovation of Spain (MICINN); and the DESI Member Institutions: https://www. desi.lbl.gov/collaborating-institutions.

The DESI Legacy Imaging Surveys consist of three individual and complementary projects: the Dark Energy Camera Legacy Survey (DECaLS), the Beijing–Arizona Sky Survey (BASS), and the Mayall *z*-band Legacy Survey (MzLS). DECaLS, BASS, and MzLS together include data obtained, respectively, at the Blanco telescope, Cerro Tololo Inter-American Observatory, NSF's NOIRLab; the Bok telescope, Steward Observatory, University of Arizona; and the

Mayall telescope, Kitt Peak National Observatory, NOIRLab. NOIRLab is operated by the Association of Universities for Research in Astronomy (AURA) under a cooperative agreement with the National Science Foundation. Pipeline processing and analyses of the data were supported by NOIRLab and the Lawrence Berkeley National Laboratory. The Legacy Surveys also use data products from the Near-Earth Object Wide-field Infrared Survey Explorer (NEOWISE), a project of the Jet Propulsion Laboratory/California Institute of Technology, funded by the National Aeronautics and Space Administration. The Legacy Surveys were supported by: the Director, Office of Science, Office of High Energy Physics of the U.S. Department of Energy; the National Energy Research Scientific Computing Center, a DOE Office of Science User Facility; the U.S. National Science Foundation, Division of Astronomical Sciences; the National Astronomical Observatories of China, the Chinese Academy of Sciences; and the Chinese National Natural Science Foundation. LBNL is managed by the Regents of the University of California under contract to the U.S. Department of Energy. The complete acknowledgments can be found at https://www.legacysurvey.org/.

Any opinions, findings, and conclusions or recommendations expressed in this material are those of the author(s) and do not necessarily reflect the views of the U.S. National Science Foundation, the U. S. Department of Energy, or any of the listed funding agencies.

The authors are honored to be permitted to conduct scientific research on Iolkam Du'ag (Kitt Peak), a mountain with particular significance to the Tohono O'odham Nation.

We also acknowledge SDSS for providing extensive spectral database support. SDSS is managed by the Astrophysical Research Consortium for the Participating Institutions of the SDSS Collaboration, including the Brazilian Participation Group, the Carnegie Institution for Science, Carnegie Mellon University, Center for Astrophysics—Harvard & Smithsonian, the Chilean Participation Group, the French Participation Group, Instituto de Astrofísica de Canarias, The Johns Hopkins University, the Kavli Institute for the Physics and Mathematics of the Universe (IPMU)/University of Tokyo, the Korean Participation Group, Lawrence Berkeley National Laboratory, Leibniz Institut für Astrophysik Potsdam (AIP), Max-Planck-Institut für Astronomie (MPIA Heidelberg), Max-Planck-Institut für Astrophysik (MPA Garching), Max-Planck-Institut für Extraterrestrische Physik (MPE), the National Astronomical Observatories of China, New Mexico State University, New York University, University of Notre Dame, Observatário Nacional/MCTI, The Ohio State University, Pennsylvania State University, Shanghai Astronomical Observatory, United Kingdom Participation Group, Universidad Nacional Autónoma de México, University of Arizona, University of Colorado Boulder, University of Oxford, University of Portsmouth, University of Utah, University of Virginia, University of Washington, University of Wisconsin, Vanderbilt University, and Yale University.

We acknowledge the efforts for public data from CTRS, PS1, PTF, and ZTF. The Catalina Sky Survey is funded by the National Aeronautics and Space Administration under grant No. NNG05GF22G, issued through the Science Mission Directorate Near-Earth Objects Observations Program. The CRTS survey is supported by the US National Science Foundation under grants AST-0909182 and AST-1313422. The CRTS survey is supported by the US National Science

Foundation under grants AST-0909182 and AST-1313422. PS1 has been made possible through contributions by the Institute for Astronomy, the University of Hawaii, the Pan-STARRS Project Office, the Max-Planck Society and its participating institutes, the Max Planck Institute for Astronomy, Heidelberg and the Max Planck Institute for Extraterrestrial Physics, Garching, The Johns Hopkins University, Durham University, the University of Edinburgh, Queen's University Belfast, the Harvard-Smithsonian Center for Astrophysics, the Las Cumbres Observatory Global Telescope Network Incorporated, the National Central University of Taiwan, the Space Telescope Science Institute, the National Aeronautics and Space Administration under grant No. NNX08AR22G issued through the Planetary Science Division of the NASA Science Mission Directorate, the National Science Foundation under grant No. AST-1238877, the University of Maryland, and Eotvos Lorand University (ELTE). PTF image data are obtained with the Samuel Oschin Telescope and the 60 inch telescope at the Palomar Observatory as part of the Palomar Transient Factory project, a scientific collaboration between the California Institute of Technology, Columbia University, Las Cumbres Observatory, the Lawrence Berkeley National Laboratory, the National Energy Research Scientific Computing Center, the University of Oxford, and the Weizmann Institute of Science. ZTF is supported by the National Science Foundation under grant No. AST-2034437 and a collaboration including Caltech, IPAC, the Weizmann Institute for Science, the Oskar Klein Center at Stockholm University, the University of Maryland, Deutsches Elektronen-Synchrotron and Humboldt University, the TANGO Consortium of Taiwan, the University of Wisconsin at Milwaukee, Trinity College Dublin, Lawrence Livermore National Laboratories, and IN2P3, France. Operations are conducted by COO, IPAC, and UW.

```
ORCID iDs
Wei-Jian Guo https://orcid.org/0000-0001-9457-0589
Hu Zou https://orcid.org/0000-0002-6684-3997
Victoria A. Fawcett https://orcid.org/0000-0003-
1251-532X
Rebecca Canning https://orcid.org/0000-0003-1398-5542
Stephanie Juneau https://orcid.org/0000-0002-0000-2394
Tamara M. Davis https://orcid.org/0000-0002-4213-8783
David M. Alexander https://orcid.org/0000-0002-
5896-6313
Linhua Jiang https://orcid.org/0000-0003-4176-6486
Steven Ahlen https://orcid.org/0000-0001-6098-7247
David Brooks  https://orcid.org/0000-0002-8458-5047
Axel de la Macorra https://orcid.org/0000-0002-1769-1640
Kevin Fanning https://orcid.org/0000-0003-2371-3356
Jaime E. Forero-Romero https://orcid.org/0000-0002-
2890-3725
Satya Gontcho A Gontcho https://orcid.org/0000-0003-
3142-233X
Theodore Kisner  https://orcid.org/0000-0003-3510-7134
Anthony Kremin https://orcid.org/0000-0001-6356-7424
Martin Landriau https://orcid.org/0000-0003-1838-8528
Aaron Meisner  https://orcid.org/0000-0002-1125-7384
Ramon Miquel https://orcid.org/0000-0002-6610-4836
John Moustakas  https://orcid.org/0000-0002-2733-4559
Jundan Nie https://orcid.org/0000-0001-6590-8122
```

Zhiwei Pan https://orcid.org/0000-0003-0230-6436

```
Francisco Prada https://orcid.org/0000-0001-7145-8674
Mehdi Rezaie https://orcid.org/0000-0001-5589-7116
Eusebio Sanchez https://orcid.org/0000-0002-9646-8198
Hee-Jong Seo https://orcid.org/0000-0002-6588-3508
Gregory Tarlé https://orcid.org/0000-0003-1704-0781
Zhimin Zhou https://orcid.org/0000-0002-4135-0977
```

References

```
Abareshi, B., Aguilar, J., Ahlen, S., et al. 2022, AJ, 164, 207
Abazajian, K. N., Adelman-McCarthy, J. K., Agüeros, M. A., et al. 2009,
   ApJS, 182, 543
Ahumada, R., Prieto, C. A., Almeida, A., et al. 2020, ApJS, 249, 3
Alam, S., Ata, M., Bailey, S., et al. 2017, MNRAS, 470, 2617
Alexander, D. M., Davis, T. M., Chaussidon, E., et al. 2023, AJ, 165, 124
Allende Prieto, C., Cooper, A. P., Dey, A., et al. 2020, RNAAS, 4, 188
Antonucci, R. 1993, ARA&A, 31, 473
Bao, D.-W., Brotherton, M. S., Du, P., et al. 2022, ApJS, 262, 14
Barth, A. J., & Bentz, M. C. 2016, MNRAS, 458, L109
Bentz, M. C., Walsh, J. L., Barth, A. J., et al. 2009, ApJ, 705, 199
Blanchard, P. K., Nicholl, M., Berger, E., et al. 2017, ApJ, 843, 106
Blandford, R. D., & McKee, C. F. 1982, ApJ, 255, 419
Bolton, A. S., Schlegel, D. J., Aubourg, É., et al. 2012, AJ, 144, 144
Brodzeller, A., Dawson, K., Bailey, S., et al. 2023, AJ, 166, 66
Cackett, E. M., Horne, K., & Winkler, H. 2007, MNRAS, 380, 669
Chambers, K. C., Magnier, E. A., Metcalfe, N., et al. 2016, arXiv:1612.05560
Chaussidon, E., Yèche, C., Palanque-Delabrouille, N., et al. 2023, ApJ,
   944, 107
Chen, Y.-J., Bao, D.-W., Zhai, S., et al. 2023, MNRAS, 520, 1807
Cohen, R. D., Rudy, R. J., Puetter, R. C., Ake, T. B., & Foltz, C. B. 1986, ApJ,
Cooper, A. P., Koposov, S. E., Allende Prieto, C., et al. 2023, ApJ, 947, 37
Denney, K. D., De Rosa, G., Croxall, K., et al. 2014, ApJ, 796, 134
DESI Collaboration, Abareshi, B., Aguilar, J., et al. 2022, AJ, 164, 207
DESI Collaboration, Adame, A. G., Aguilar, J., et al. 2023a, arXiv:2306.06308
DESI Collaboration, Adame, A. G., Aguilar, J., et al. 2023b, arXiv:2306.06307
DESI Collaboration, Aghamousa, A., Aguilar, J., et al. 2016a, arXiv:1611.
   00036
DESI Collaboration, Aghamousa, A., Aguilar, J., et al. 2016b, arXiv:1611.
Dexter, J., & Agol, E. 2011, ApJL, 727, L24
Dey, A., Schlegel, D. J., Lang, D., et al. 2019, AJ, 157, 168
Drake, A. J., Djorgovski, S. G., Mahabal, A., et al. 2009, ApJ, 696, 870
Du, P., Brotherton, M. S., Wang, K., et al. 2018, ApJ, 869, 142
Du, P., & Wang, J.-M. 2019, ApJ, 886, 42
Eisenstein, D. J., Weinberg, D. H., Agol, E., et al. 2011, AJ, 142, 72
Elitzur, M., & Ho, L. C. 2009, ApJL, 701, L91
Elitzur, M., Ho, L. C., & Trump, J. R. 2014, MNRAS, 438, 3340
Esin, A. A., McClintock, J. E., & Narayan, R. 1997, ApJ, 489, 865
Fawcett, V. A., Alexander, D. M., Rosario, D. J., et al. 2020, MNRAS,
   494, 4802
Fawcett, V. A., Alexander, D. M., Rosario, D. J., et al. 2022, MNRAS,
   513, 1254
Feng, H.-C., Hu, C., Li, S.-S., et al. 2021, ApJ, 909, 18
Fitzpatrick, E. L. 1999, PASP, 111, 63
Flaugher, B., Diehl, H. T., Honscheid, K., et al. 2015, AJ, 150, 150
Frederick, S., Gezari, S., Graham, M. J., et al. 2019, ApJ, 883, 31
Gezari, S., Hung, T., Cenko, S. B., et al. 2017, ApJ, 835, 144
Glikman, E., LaMassa, S., Piconcelli, E., Urry, M., & Lacy, M. 2017, ApJ,
Goddard, Q. E., Bastian, N., & Kennicutt, R. C. 2010, MNRAS, 405, 857
Graham, M. J., Ross, N. P., Stern, D., et al. 2020, MNRAS, 491, 4925
Green, P. J., Pulgarin-Duque, L., Anderson, S. F., et al. 2022, ApJ, 933, 180
Gunn, J. E., Siegmund, W. A., Mannery, E. J., et al. 2006, AJ, 131, 2332
Guo, H., Peng, J., Zhang, K., et al. 2020, ApJ, 905, 52
Guo, H., Sun, M., Liu, X., et al. 2019, ApJL, 883, L44
Guo, W.-J., Li, Y.-R., Zhang, Z.-X., Ho, L. C., & Wang, J.-M. 2022, ApJ, 929, 19
```

```
Guy, J., Bailey, S., Kremin, A., et al. 2023, AJ, 165, 144
Hahn, C., Wilson, M. J., Ruiz-Macias, O., et al. 2023, AJ, 165, 253
Ho, L. C. 2005, arXiv:astro-ph/0511157
Ho, L. C., & Kim, M. 2014, ApJ, 789, 17
Hon, W. J., Wolf, C., Onken, C. A., Webster, R., & Auchettl, K. 2022,
         S, 511, 54
Hu, C., Li, S.-S., Guo, W.-J., et al. 2020, ApJ, 905, 75
Jin, J.-J., Wu, X.-B., & Feng, X.-T. 2022, ApJ, 926, 184
Kaspi, S., Smith, P. S., Netzer, H., et al. 2000, ApJ, 533, 631
Klindt, L., Alexander, D. M., Rosario, D. J., Lusso, E., & Fotopoulou, S. 2019,
           5, 488, 3109
LaMassa, S. M., Cales, S., Moran, E. C., et al. 2015, ApJ, 800, 144
Lan, T.-W., Tojeiro, R., Armengaud, E., et al. 2023, ApJ, 943, 68
Law, N. M., Kulkarni, S. R., Dekany, R. G., et al. 2009, PASP, 121, 1395
Levi, M., Bebek, C., Beers, T., et al. 2013, arXiv:1308.0847
Li, R., Ho, L. C., Ricci, C., et al. 2022a, ApJ, 933, 70
Li, S.-S., Feng, H.-C., Liu, H. T., et al. 2022b, ApJ, 936, 75
Li, Y.-R., Songsheng, Y.-Y., Qiu, J., et al. 2018, ApJ, 869, 137
Lu, K.-X., Wang, J.-G., Zhang, Z.-X., et al. 2021, ApJ, 918, 50
Lyke, B. W., Higley, A. N., McLane, J. N., et al. 2020, ApJS, 250, 8
MacLeod, C. L., Green, P. J., Anderson, S. F., et al. 2019, ApJ, 874, 8
MacLeod, C. L., Ross, N. P., Lawrence, A., et al. 2016, MNRAS, 457, 389
Masci, F. J., Laher, R. R., Rusholme, B., et al. 2019, PASP, 131, 018003
Matt, G., Guainazzi, M., & Maiolino, R. 2003, MNRAS, 342, 422
Miller, T. N., Doel, P., Gutierrez, G., et al. 2023, arXiv:2306.06310
Myers, A. D., Moustakas, J., Bailey, S., et al. 2023, AJ, 165, 50
Noda, H., & Done, C. 2018, MNRAS, 480, 3898
Osterbrock, D. E. 1981, ApJ, 249, 462
Peterson, B. M. 1993, PASP, 105, 247
Planck Collaboration, Aghanim, N., Akrami, Y., et al. 2020, A&A,
Raichoor, A., Moustakas, J., Newman, J. A., et al. 2023, AJ, 165, 126
Ricci, C., & Trakhtenbrot, B. 2023, NatAs, 7, 1282
Richards, G. T., Kruczek, N. E., Gallagher, S. C., et al. 2011, AJ, 141, 167
Rogerson, J. A., Hall, P. B., Ahmed, N. S., et al. 2018, ApJ, 862, 22
Ross, N. P., Graham, M. J., Calderone, G., et al. 2020, MNRAS, 498, 2339
Ruiz-Macias, O., Zarrouk, P., Cole, S., et al. 2020, RNAAS, 4, 187
Runnoe, J. C., Cales, S., Ruan, J. J., et al. 2016, MNRAS, 455, 1691
Schlafly, E. F., Kirkby, D., Schlegel, D. J., et al. 2023, AJ, 166, 259
Shakura, N. I., & Sunyaev, R. A. 1973, A&A, 500, 33
Shapovalova, A. I., Popović, L. Č., Burenkov, A. N., et al. 2010, A&A,
  509, A106
Sheng, Z., Wang, T., Jiang, N., et al. 2017, ApJL, 846, L7
Silber, J. H., Fagrelius, P., Fanning, K., et al. 2023, AJ, 165, 9
Smee, S. A., Gunn, J. E., Uomoto, A., et al. 2013, AJ, 146, 32
Śniegowska, M., & Czerny, B. 2020, A&A, 641, A167
Stacey, H. R., Costa, T., McKean, J. P., et al. 2022, MNRAS, 517, 3377
Stoughton, C., Lupton, R. H., Bernardi, M., et al. 2002, AJ, 123, 485
Sun, M., Xue, Y., Richards, G. T., et al. 2018, ApJ, 854, 128
Temple, M. J., Ricci, C., Koss, M. J., et al. 2023, MNRAS, 518, 2938
Tie, S. S., & Kochanek, C. S. 2018, MNRAS, 473, 80
Vanden Berk, D. E., Wilhite, B. C., Kron, R. G., et al. 2004, ApJ, 601, 692
Wang, J.-M., & Bon, E. 2020, A&A, 643, L9
Wang, J.-M., & Zhang, E.-P. 2007, ApJ, 660, 1072
Winkler, H. 1992, MNRAS, 257, 677
Yan, L., Wang, T., Jiang, N., et al. 2019, ApJ, 874, 44
Yang, Q., Green, P. J., MacLeod, C. L., et al. 2023, ApJ, 953, 61
Yang, Q., Wu, X.-B., Fan, X., et al. 2018, ApJ, 862, 109
Yèche, C., Palanque-Delabrouille, N., Claveau, C.-A., et al. 2020, RNAAS,
Yi, W., Brandt, W. N., Ni, Q., et al. 2022, ApJ, 930, 5
Yu, Z., Martini, P., Penton, A., et al. 2021, MNRAS, 507, 3771
Zeltyn, G., Trakhtenbrot, B., Eracleous, M., et al. 2022, ApJL, 939, L16
Zhang, X.-G., & Feng, L.-L. 2016, MNRAS, 457, 3878
Zhang, Z.-X., Du, P., Smith, P. S., et al. 2019, ApJ, 876, 49
Zhou, R., Dey, B., Newman, J. A., et al. 2023, AJ, 165, 58
Zhou, R., Newman, J. A., Dawson, K. S., et al. 2020, RNAAS, 4, 181
Zhuang, M.-Y., & Ho, L. C. 2019, ApJ, 882, 89
Zou, H., Zhang, T., Zhou, Z., et al. 2018, ApJS, 237, 37
```